nature neuroscience

Article

https://doi.org/10.1038/s41593-026-02378-x

Microglia prune developing cortical blood vessels through PD-1 signaling

Received: 23 October 2024

Accepted: 12 June 2026

Published online: 16 July 2026

Check for updates

Mengtian Zhang[1,2,3,6], Yanyan Wang[1,2,6], Runhua Yang[1,2], Fen Ji[1,2], Sihan Li[1,2], Chenxiao Li[1,2,4], Xinghua Zhao[1,2,5], Hong Li[1,2] & Jianwei Jiao[1,2]

During cerebrovascular development, an initial surplus of vessels is generated and subsequently refined through selective elimination to establish an efficient vascular network. Microglia are pivotal regulators of synaptic refinement and brain circuitry maturation, and despite their close interactions with cerebral vessels, whether and how they contribute to cerebrovascular pruning remains unclear. Here, to address this, we visualized and manipulated microglia–vessel interactions in the frontal cortex of postnatal day 11 mice. We found that microglia progressively approach cerebral vessels and subsequently mediate their pruning. Furthermore, we identify the PD-L1–PD-1 signaling axis as a regulator of microglia-mediated vascular pruning via microglial CD5L secretion. Altogether, our findings uncover a role for microglia in targeting redundant vasculature to facilitate vascular network formation during brain development.

During brain development, microglia dynamically extend and retract their highly branched processes to constantly survey the brain microenvironment. Accumulating evidence demonstrates that microglia contribute to neural network establishment in the developing brain by promoting neurogenesis, mediating synaptic pruning, facilitating neuronal apoptosis and phagocytosing cellular debris[1]. Additionally, microglia phagocytose myelin to restrict myelin overdevelopment and regulate myelin refinement through sheath pruning during development[2]. Microglia maintain close physical proximity to cerebral vessels, serving as a critical component of the cerebral vascular niche[3]. They are also involved in regulating vascular patency and diameter, cerebral blood flow, blood–brain barrier integrity, clearance of vascular calcifications and the survival of brain endothelial cells (ECs)[4]. The interaction between microglia and cerebral blood vessels is dynamic and continuous. Previous studies have shown that juxtavascular microglia exhibit heightened activity during the early postnatal period. Microglia can migrate within the developing brain parenchyma by utilizing the vascular network, but this migratory capacity is constrained upon the maturation of astrocyte endfeet[5]. In a traumatic brain injury model, the motility of juxtavascular microglia is substantially enhanced compared to the naive state[6]. These studies suggest that perivascular microglia exert a mysterious role in brain physiology. During development, cerebral blood vessels undergo angiogenesis and vascular pruning. While the function of microglia in angiogenesis has been explored, their functional relevance in cerebrovascular pruning remains elusive.

Programmed cell death protein 1 (PD-1, also known as CD279) is encoded by the *Pdcd1* gene, which is a member of the CD28 superfamily. As an immune checkpoint receptor, PD-1 is upregulated on activated T cells to induce immune tolerance[7,8]. Recent studies have revealed that PD-1 also exerts active role in the central and peripheral nervous systems[9]. The canonical ligands of PD-1 are CD274 (PD-L1) and PDCD1LG2 (PD-L2); however, their functional roles in the brain differ substantially. Among these ligand–receptor interactions, the PD-L1–PD-1 axis has emerged as a pivotal focus in recent brain research[10]. In hippocampal excitatory neurons, the PD-L1–PD-1 axis modulates neuronal excitability and synaptic plasticity, thereby influencing learning

[1]State Key Laboratory of Organ Regeneration and Reconstruction, Institute of Zoology, Chinese Academy of Science, Beijing, China. [2]University of Chinese Academy of Sciences, Beijing, China. [3]Department of Anesthesiology, Second Clinical Medicine College, Shandong Medical And Pharmaceutical University, Yantai, China. [4]Affiliated Hospital of Guangdong Medical University & Key Laboratory of Zebrafish Model for Development and Disease of Guangdong Medical University, Zhanjiang, China. [5]China Japan Union Hospital, Jilin University, Changchun, China. [6]These authors contributed equally: Mengtian Zhang, Yanyan Wang. e-mail: jwjiao@ioz.ac.cn

and memory functions[10]. During mouse brain development, the PD-L1–PD-1 signaling pathway modulates the morphological complexity of astrocytes, increasing vascular endfoot coverage. This impairs the vascular-associated migration of oligodendrocyte precursor cells and ultimately results in cognitive impairment in mice. Furthermore, the PD-L1–PD-1 axis has been implicated in central nervous system (CNS) disorders including brain tumors, Alzheimer's disease (AD), cognitive dysfunction and pain[11–13]. In patients with AD and APP/PS1 mouse models, astrocytic PD-L1 and microglial PD-1 are upregulated around amyloid-β (Aβ) plaques. Astrocyte-derived PD-L1 undergoes juxtamembrane shedding to activate microglial PD-1, suppressing neuroinflammation and promoting Aβ uptake[14]. Moreover, in pain-sensing neurons, the PD-L1–PD-1 signaling axis modulates neuronal excitability by regulating the functional activity of K^+ channels, identifying PD-L1 as an endogenous pain inhibitor and neuromodulator[12]. Immune-related molecules secreted by microglia are key regulators of developmental synapse elimination. Recent studies have identified many critical immune signals that govern microglia-mediated synaptic pruning, including CX3CL1–CX3CR1, IL-33–ST2, JAK2–STAT1 and DAP12–TREM2-mediated signaling[15,16]. Therefore, we were interested in whether PD-1 might play an important role in microglia targeting cerebral vessels.

In this study, we investigated microglia-cerebral vasculature interactions in vivo using a mouse model. We found that microglia, which tend to enwrap cerebral vessels, perform auxiliary pruning of cerebral vasculature during vascular remodeling. Specifically, the PD-L1–PD-1 axis engages the SHP-1-regulated Erk1/2–mTOR signaling pathway in microglia, thereby modulating their phagocytic capacity. Meanwhile, PD-1 instructs microglia to target cerebral vasculature more precisely by secreting CD5L (CD5 antigen-like precursor) proteins. Our findings establish that microglia contribute to cerebrovascular pruning, expanding our mechanistic understanding of cerebral vascular development.

Results

Microglia associate with cerebral vasculature during brain development

During early brain development, microglia contribute to the cerebral vascular niche through physical proximity, and their shared role in maintaining CNS tissue homeostasis makes them natural functional partners[3]. The mouse cerebral cortex is divided into the frontal cortex, parietal cortex, temporal cortex and occipital cortex. As the frontal cortex is responsible for higher cognitive functions, we focus on the interaction between microglia and cerebral blood vessels in the frontal cortex. Therefore, we evaluated the positional relationship between microglia and cerebral vessels in the frontal cortex by using high-power confocal microscope and found two types of microglia: nonvessel-associated microglia (NVAM; less than 30%) and vessel-associated microglia (VAM; more than 30%). Among these, VAM emerged as a key focus of our investigation (Fig. 1a and Extended Data Fig. 1a–b). Notably, VAM exhibited markedly increased lysosomal content compared to NVAM (Fig. 1b,c). Postnatal days 0–14 (P0–P14) are established as the critical period for cerebral cortical vascular remodeling[17]. We found that microglial association with cerebral vessels in different degrees, and P11 was the most obvious, which indicated that P11 was the key stage for microglia–vascular crosstalk (Fig. 1d,e). Super-resolution imaging and three-dimensional (3D) reconstruction revealed an enrichment of $CD68^+$ lysosomes in microglia around cerebral vessels at P11, which indicated that these microglia had high phagocytic activity (Fig. 1f,g). To examine microglia–vascular interactions, we used *Cx3cr1*$^{GFP/+}$ reporter mice, in which microglia were selectively labeled with GFP[18]. Simultaneously, *Cx3cr1*$^{GFP/+}$ mice were crossed with *Tie2*-Cre::Ai14 mice to obtain *Tie2*-Cre::Ai14::*Cx3cr1*$^{GFP/+}$ mice, where vessels are labeled with tdTomato, enabling high-resolution visualization of microglia–vascular interactions (Fig. 1h). The imaging experiments showed that some cerebral vessels were progressively associated with microglia (Fig. 1i,j and Supplementary Videos 1–4). Microglia-associated vessels exhibited smaller diameters compared to nonmicroglia-associated vessels (Fig. 1k). Furthermore, we found that the diameter of cerebral blood vessels associated with microglia is approximately 2–4 μm, suggesting that these microglia-interacting vessels are likely to be cortical capillaries (Fig. 1k). All together, these results demonstrate that microglia are closely related to the cerebral vessels development.

Microglia assist cerebrovascular remodeling during development

To determine whether microglia are required for cerebral vascular development, we assessed cerebral vascular morphology following microglial depletion. We administered the colony-stimulating factor 1 receptor (CSF-1R) inhibitor PLX5622 daily from postnatal day 7 (P7) to P14, which effectively depleted microglia (Extended Data Fig. 1c). Of note, we found that the length and branch point number of cerebral vessels increased in microglia deletion compared to controls (Extended Data Fig. 1d–g). To evaluate blood–brain barrier integrity, we performed immunofluorescence staining and quantification of the tight junction markers Claudin-5 and ZO1, and the results indicated that there were no changes after microglia deletion (Extended Data Fig. 1h–k). Recent studies have shown that microglial depletion via CSF-1R inhibitors exacerbates neuronal excitotoxicity and enhances neural activity, which may indirectly affect cerebral vasculature[19]. To further assess the effects of microglia on the cerebral vasculature, we used *Tie* CreER::R26-DTR transgenic mice to specifically deplete microglia via diphtheria toxin (DT). Mice received intraperitoneal tamoxifen injections for 3 consecutive days from P0 to P3. Subsequently, intracerebroventricular (ICV) injections of PBS or DT were administered daily from P10 to P12, and brain tissue was collected on P13 (Fig. 2a). $IBA1^+$ cells were markedly reduced in the cerebral cortex of DT-treated mice compared to PBS controls (Fig. 2b,c). Consistent with PLX5622-mediated depletion, DT-treated mice exhibited increased cerebral vessel branch point number and total length, implying that microglia were involved in cerebral vascular remodeling (Fig. 2b,d,e).

To determine whether microglia directly interact with cerebral vasculature during development, we performed in vivo imaging using super-resolution confocal microscopy. Compared to nonmicroglia-associated cerebral vessels, those associated with microglia gradually disappear over time (Fig. 2f–h and Supplementary Videos 5–8). Notably, not all VAM exhibited auxiliary pruning functions. Among them, some microglia left the cerebral vessels, whereas others maintained an association and mediated pruning (Extended Data Fig. 2a–c and Supplementary Videos 9–12). We found that the proportion of microglia leaving and associating with cerebral vessels was similar (Extended Data Fig. 2d). To further assess the functional role of microglial activity in pruning, we intravenously injected Tuftsin to activate microglia before in vivo imaging (Fig. 2i and Extended Data Fig. 2e). Activated microglia accelerated cerebral vascular pruning (Fig. 2j,k and Extended Data Fig. 2f–h). Consistent with this, immunofluorescence staining revealed increased $CD68^+$ lysosomes in VAM following Tuftsin injection, indicating enhanced phagocytic capacity (Extended Data Fig. 2i,j). Together, these live-imaging and functional experiments demonstrate that microglia assist cerebral vascular remodeling by pruning redundant cerebral vessels during development.

PD-1 deficiency disrupts microglia phagocytosis

Recent studies have shown that in addition to immune cells, microglia and neurons in the CNS also widely express PD-1 (refs. 12,20). We performed quantitative PCR with reverse transcription to analyze the expression of *Pd-1* in different brain cell types during development. Results showed that *Pd-1* was expressed in all cell types at varying levels, with the highest expression in microglia (Fig. 3a). Treatment of primary

https://doi.org/10.1038/s41593-026-02378-x

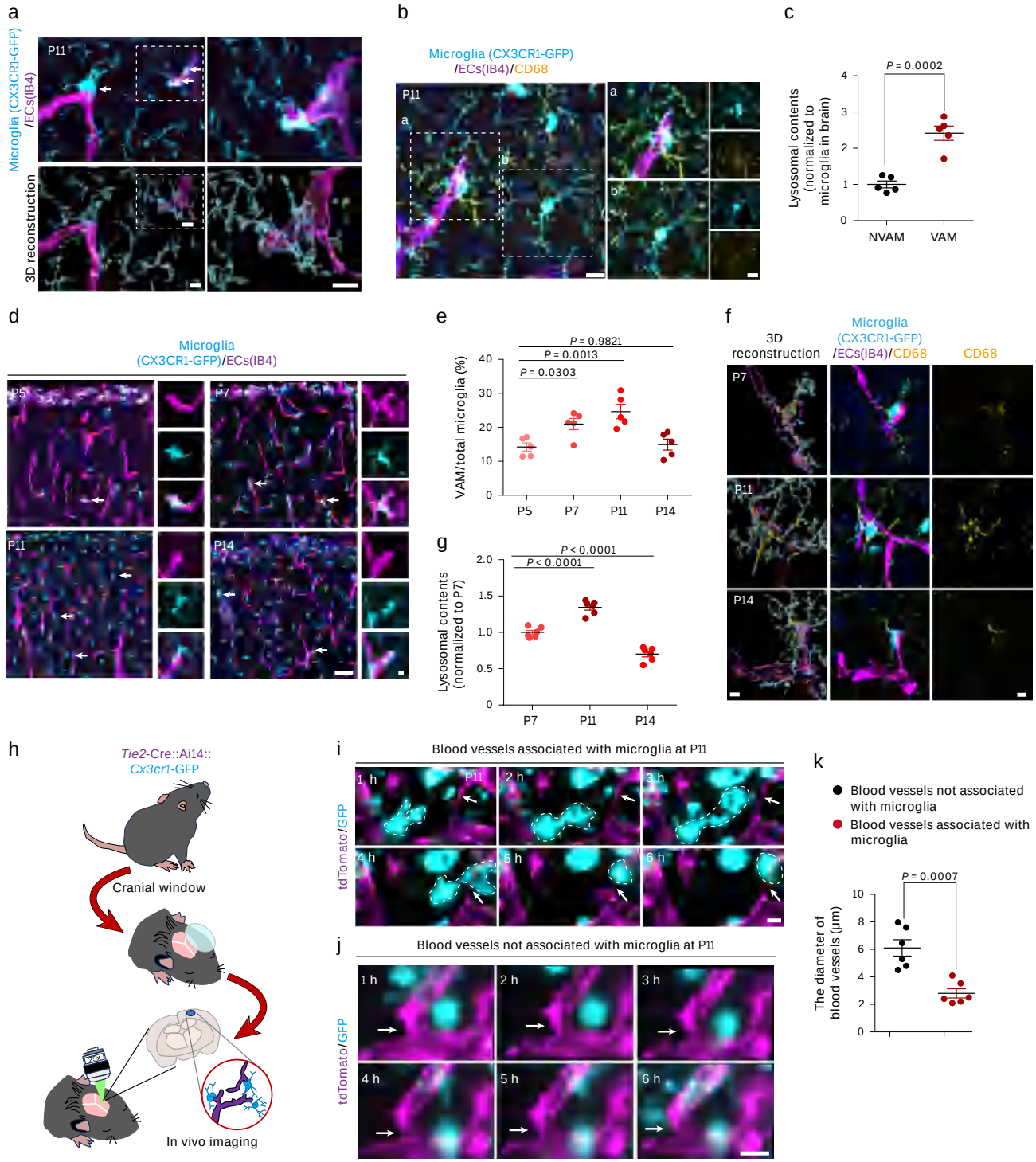

Fig. 1 | VAM exhibit a higher activation state compared to NVAM. a, Confocal images and reconstructions of microglia (GFP, blue) and cerebral vessels (IB4, purple) at P11. White arrowheads, VAM. The right insets indicated higher magnification images of the delineated areas. Scale bars, 5 μm. These results were independently repeated in three separate experiments from three mice, and consistent findings were obtained. **b**, Images and reconstruction of microglia (GFP, blue) containing lysosomes (CD68, yellow) at P11. The images on the right were enlarged versions. Scale bars, 10 μm. **c**, Quantification of lysosomal contents in NVAM and VAM (CD68 immunoreactivity per cell) for **b**. $n = 5$ cells from five mice. **d**, Representative images of the relationship between microglia and cerebral vessels during P5, P7, P11 and P14. White arrowheads, VAM. Scale bars, 50 μm (overview) and 5 μm (inset and rendering). **e**, The proportion of VAM among all microglia at P5, P7, P11 and P14. $n = 5$ mice per group. **f**, Images and reconstruction of microglia containing lysosomes at P7, P11 and P14. Scale bars, 5 μm. **g**, Quantification of lysosomal contents in VAM at P7, P11 and P14. $n = 6$ cells from six mice. **h**, For in vivo imaging, an optical window was opened on the skull in *Tie2*-Cre::Ai14::*Cx3cr1*$^{GFP/+}$ mice at P11. **i**,**j**, Time-lapse imaging captured the dynamics of microglia associating with and not associating with the cerebral vasculature at P11. Scale bars, 10 μm. **k**, Quantification of cerebral vascular diameter associated or not associated with microglia. $n = 6$ blood vessels from six mice. NVAM, the proportion of the overlapping volume between microglia and cerebral blood vessels to the total volume of microglia was less than 30%; VAM, the proportion of the overlapping volume between microglia and cerebral blood vessels to the total volume of microglia was more than 30%. For **c** and **k**, data were analyzed using a two-tailed unpaired *t*-test. For **e** and **g**, data were analyzed using a one-way analysis of variance (ANOVA) with Dunnett's test. Data are presented as mean ± s.e.m. for **c**, **e**, **k** and **g**.

https://doi.org/10.1038/s41593-026-02378-x

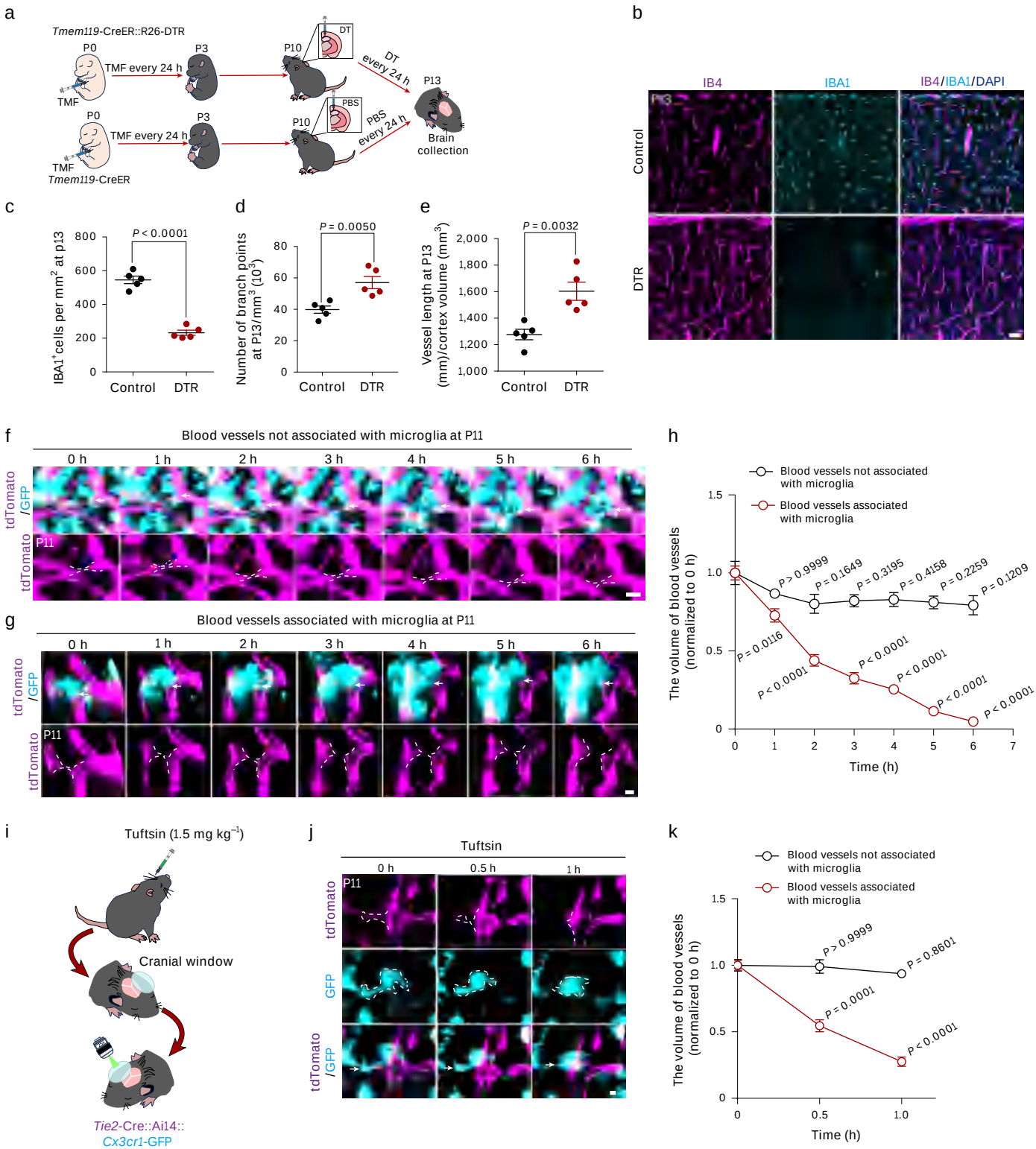

Fig. 2 | Microglia interact with cerebral vessels during development. **a**, Schematic representation of microglia ablation in *Tmem119*-CreER::R26-DTR mice. *Tmem119*-CreER mice were used as controls. TMF, tamoxifen. **b**, Immunofluorescence staining for IB4 and IBA1 in control and DTR mice. Scale bars, 50 µm. **c**, The graph showed significantly decreased IBA1$^+$ cells in DTR mice at P13. $n = 5$ brain slices from five mice. **d**,**e**, Quantification of the number of branch points (**d**) and the vessels length (**e**) in control and DTR mice at P13. $n = 5$ brain slices from five mice. **f**, The changes of cerebral vessels not associated with microglia during 6 h. Scale bars, 10 µm. **g**, The changes of cerebral vessels associated with microglia during 6 h. Scale bars, 10 µm. **h**, Quantitative analysis of cerebral vascular volume. $n = 5$ mice per group. **i**, For in vivo imaging, *Tie2*-Cre::Ai14::*Cx3cr1*$^{GFP/+}$ mice were injected with Tuftsin (1.5 mg kg^{-1}) intravenously in the temporal (or facial) and craniotomy was performed. **j**, Time-lapse images of cerebral vessels associated with microglia after intravenous injection of Tuftsin in *Tie2*-Cre::Ai14::*Cx3cr1*$^{GFP/+}$ mice at P11. Scale bars, 10 µm. **k**, Quantification of cerebral vessels after intravenous injection of Tuftsin. $n = 5$ mice per group. For **c**–**e**, data were analyzed using a two-tailed unpaired *t*-test. For **h** and **k**, data were analyzed using a repeated-measures two-way ANOVA with Bonferroni's test. Data are presented as mean ± s.e.m. for **c**–**e**, **h** and **k**.

microglia with the activator Tuftsin increased the expression of CD68 and PD-1, indicating that PD-1 is associated with microglial activation (Fig. 3b–d). To further investigate the important function of PD-1 on microglia, we used *Pd-1*$^{flox/flox}$ (*Pd-1*$^{fl/fl}$) mice crossed with *Cx3cr1*-Cre mice to generate microglial *Pd-1* conditional knockout mice (cKO) (*Pd-1*$^{cKO\text{-}Cx3}$) (Fig. 3e). Western blotting indicated that the expression of PD-1 was specifically reduced in *Pd-1*$^{cKO\text{-}Cx3}$ microglia (Fig. 3f,g). Then, qPCR analysis of primary microglia confirmed that the abundance of *Pd-1* mRNA was greatly decreased in *Pd-1*$^{cKO\text{-}Cx3}$ brain cortex, which was consistent with western blot results (Fig. 3h). Immunofluorescence staining for CD68 and PD-1 demonstrated that PD-1 deficiency altered lysosomal content in IBA1$^+$ cells (Extended Data Fig. 3a–c). Three-dimensional reconstructions further showed reduced lysosomal content in vessel-associated IBA1$^+$ cells from *Pd-1*$^{cKO\text{-}Cx3}$ mice, suggesting impaired phagocytic activity (Fig. 3i,j).

As CX3CR1 and IBA1 label both microglia and monocyte-derived macrophages, they lack microglia specificity. We therefore used *Tmem119*-CreER mice, which selectively target yolk sac-derived microglia but not other macrophage populations[21]. We crossed *Tmem119*-CreER mice with *Pd-1*$^{fl/fl}$ and Ai14 mice to obtain *Pd-1*$^{cKO\text{-}TmemER}$::Ai14 mice. In this model, tamoxifen-induced Cre activation mediates microglia-specific *Pd-1* knockout and tdTomato expression (red fluorescence) in microglia (Extended Data Fig. 3d). Consistent with previous results, PD-1 deficiency reduced CD68 expression (Extended Data Fig. 3e,f). To link PD-1 loss directly to impaired phagocytosis, we assessed phagocytic capacity in isolated *Pd-1*$^{fl/fl}$ and *Pd-1*$^{cKO\text{-}Cx3}$ microglia via beads co-culture assays. *Pd-1*$^{cKO\text{-}Cx3}$ microglia exhibited markedly reduced beads phagocytosis compared to *Pd-1*$^{fl/fl}$ controls (Fig. 3k,l). For in vivo validation, we performed functional phagocytosis assays using pHrodo Red-conjugated particles[22]. Acute brain slices from *Pd-1*$^{fl/fl}$ and *Pd-1*$^{cKO\text{-}Cx3}$ mice were exposed to these pH-sensitive particles, and results confirmed reduced phagocytosis in PD-1-deficient microglia, which was consistent with in vitro results (Fig. 3m–o). In conclusion, our results show that PD-1 is essential for maintaining phagocytic function in microglia during development.

PD-1 has two canonical ligands, PD-L1, which is broadly expressed in immune and nonimmune cells, and PD-L2, whose expression is more restricted to immune cells[13]. We detected the release of PD-L1 and PD-L2 by using a mouse brain slice preparation (Extended Data Fig. 3g). Enzyme-linked immunosorbent assay (ELISA) results showed that PD-L1 and PD-L2 release was unaltered in brain slices from *Pd-1*$^{cKO\text{-}Cx3}$ mice (Extended Data Fig. 3h,i). Subsequently, to assess the functional effects of these ligands on microglial phagocytosis, we added recombinant PD-L1 or PD-L2 protein to co-cultures of isolated primary microglia and fluorescent beads. Immunofluorescence staining results showed that PD-L1 protein enhanced the phagocytic ability of IBA1$^+$ cells, and this ability disappeared after PD-1 deficiency (Extended Data Fig. 4a–c). To identify the ligand driving microglial targeting of cerebral vessels, we administered PD-L1 or PD-L2 protein via ICV injection (Extended Data Fig. 4d). Exogenous PD-L1 increased the number of vessel-associated IBA1$^+$ cells (Extended Data Fig. 4e–g), indicating that PD-L1 may act through PD-1 to direct IBA1$^+$ cells to survey cerebral vasculature. We further investigated the interaction between PD-L1 and PD-L2 with PD-1 through functional deficiency experiments (anti-PD-L1 monoclonal antibody and anti-PD-L2 monoclonal antibody treatments). Anti-PD-L1 monoclonal antibody or anti-PD-L2 monoclonal antibody was injected daily into the brain ventricles from P10 to P13 (Extended Data Fig. 4h). Anti-PD-L1 monoclonal antibody treatment increased cerebral vessel length and branch point number in *Pd-1*$^{fl/fl}$ mice, but this phenotype was absent in *Pd-1*$^{cKO\text{-}Cx3}$ mice (Extended Data Fig. 4i–m). In contrast, anti-PD-L2 monoclonal antibody had no effect on vascular morphology. Collectively, these data demonstrate that the PD-L1–PD-1 axis specifically mediates microglial pruning of cerebral vessels.

PD-1 deficiency impairs microglial pruning of cerebral vasculature

Considering that PD-1 deficiency causes a reduction in microglia phagocytosis, we wondered whether this defect affects cerebral vascular development. To visualize the dynamic changes of microglia, we crossed *Pd-1*$^{fl/fl}$ mice with *Cx3cr1*-CreER and Ai14 mice to generate microglia-specific *Pd-1* conditional knockout mice (*Pd-1*$^{cKO\text{-}Cx3ER}$::Ai14), which express tdTomato (red fluorescence) following 3 days of tamoxifen induction (Fig. 4a). We found that tdTomato only specifically labeled IBA1$^+$ cells, but not CD31$^+$ ECs, NeuN$^+$ neurons and GFAP$^+$ astrocytes (Extended Data Fig. 5a). The 3D reconstruction results revealed reduced lysosomal content in VAM from *Pd-1*$^{cKO\text{-}cx3ER}$::Ai14 mice compared to *Cx3Cr1*-CreER::Ai14 mice (Fig. 4b,c). To assess vascular pruning dynamics, we intravenously injected DyLight 488 to label cerebral vessels and performed in vivo time-lapse confocal imaging in *Cx3cr1*-CreER::Ai14 and *Pd-1*$^{cKO\text{-}Cx3ER}$::Ai14 mice (Fig. 4d). The results showed that microglia progressively pruned cerebral vessels, leading to their detachment from the main vascular network, but the effect substantially attenuated by *Pd-1* deficiency (Fig. 4e–g and Supplementary Videos 13 and 16). We further observed that VAM in both genotypes segregated into two subpopulations: those that persistently associated with vessels and those that left (Fig. 4e,f and Extended Data Fig. 5b,c). At the same time, immunofluorescence staining also showed that VAM were reduced in *Pd-1*$^{cKO\text{-}cx3ER}$::Ai14 cerebral cortex (Extended Data Fig. 5d,e). During early development, microglia sense neuronal activity to actively prune immature synapses. To further explore the role of *Pd-1*-deficient microglia on neurons, we quantified synaptic proteins in *Pd-1*$^{fl/fl}$ and *Pd-1*$^{cKO\text{-}Cx3}$ brain. Levels of Synapsin1 and Homer1 (synapse-associated proteins) were unaltered following microglia-specific *Pd-1* deletion, indicating *Pd-1*-deficient microglia do not affect synaptic pruning (Extended Data Fig. 5f,g). Western blotting revealed increased levels of the autophagy marker P62 and decreased

Fig. 3 | PD-1 correlates with microglia phagocytosis during development. **a**, *Pd-1* mRNA levels were detected in microglia, NPCs, neurons, ECs and astrocytes. *Gapdh* was an internal reference gene. NPCs, neural precursor cells. $n = 5$ mice per group. **b**, Immunofluorescence staining for primary microglia labeled for IBA1, CD68 and PD-1. Scale bars, 5 µm. **c**,**d**, Quantification of CD68$^+$ fluorescence (**c**) and PD-1$^+$ fluorescence (**c**) in primary microglia treated with saline and Tuftsin. $n = 6$ cells from six mice. **e**, Schematic of the microglial *Pd-1* cKO mouse construction strategy. LoxP sites were inserted between the second and fourth exons in these mice. The *Pd-1* gene was knocked out by microglia-specific Cre recombinase splicing. **f**, Western blot analysis showed that the protein levels of PD-1 were reduced in the microglia of *Pd-1*$^{cKO\text{-}Cx3}$ mice. β-actin was used as loading control. **g**, Bar graph shows the normalized densitometry of PD-1. $n = 4$ mice per group. **h**, qPCR analysis of relative *Pd-1* mRNA abundance in the *Pd-1*$^{fl/fl}$ and *Pd-1*$^{cKO\text{-}Cx3}$ microglia. $n = 4$ mice per group. **i**, Images and reconstructions of the lysosomal contents (CD68, yellow) in microglia (IBA1, blue) enwrapping cerebral vessels (IB4, purple) in the *Pd-1*$^{fl/fl}$ and *Pd-1*$^{cKO\text{-}Cx3}$ mice at P11. Scale bars, 10 µm. The right insets indicated higher magnification images of the delineated areas. Scale bars, 5 µm. **j**, Quantification of the lysosomal contents in *Pd-1*$^{fl/fl}$ and *Pd-1*$^{cKO\text{-}Cx3}$ microglia around cerebral vessels. $n = 7$ cells from seven mice. **k**, Primary microglial were incubated with fluorescent microbeads (blue) for 4 h and stained with phalloidin (purple). Scale bars, 5 µm. DAPI, 4,6-diamidino-2-phenylindole. **l**, Quantitative analysis of the number of fluorescent microbeads in each cell. $n = 13$ cells from 13 mice. **m**, Schematic representation of microglia phagocytosis determined by slice culturing system. **n**, Phagocytosis on slice culture sections showed that fewer pH-sensitive beads were engulfed by *Pd-1*$^{cKO\text{-}Cx3}$ microglia at P11. Scale bars, 50 µm. **o**, Quantification analysis of the microglia phagocytosis assay in **n**. $n = 5$ brain slices from five mice. For **a**, data were analyzed using a one-way ANOVA with Dunnett's test. For **c**,**d**,**g**,**h**,**j**,**l**,**o**, data were analyzed using a two-tailed unpaired *t*-test. Data are presented as mean ± s.e.m. for **a**,**c**,**d**,**g**,**h**,**j**,**l**,**o**.

https://doi.org/10.1038/s41593-026-02378-x

LC3-II in *Pd-1*$^{cKO\text{-}Cx3}$ microglia, suggesting that *Pd-1* deficiency impairs autophagy-related phagocytosis in IBA1$^+$ cells (Extended Data Fig. 5h,i). Meanwhile, similar results were obtained by immunohistochemistry (Extended Data Fig. 5j,k). Together, these results indicate that PD-1 drives IBA1$^+$ cells to assist cerebrovascular pruning.

PD-1-directed microglial mediation of cerebral vascular pruning persists during vascular remodeling

To investigate the changes of cerebral vessels, co-immunostaining of CD31 with IBA1 was performed in *Pd-1*$^{fl/fl}$ and *Pd-1*$^{cKO\text{-}Cx3}$ brain cortex at P11 (Fig. 5a). Results showed reduced total IBA1$^+$ cell abundance

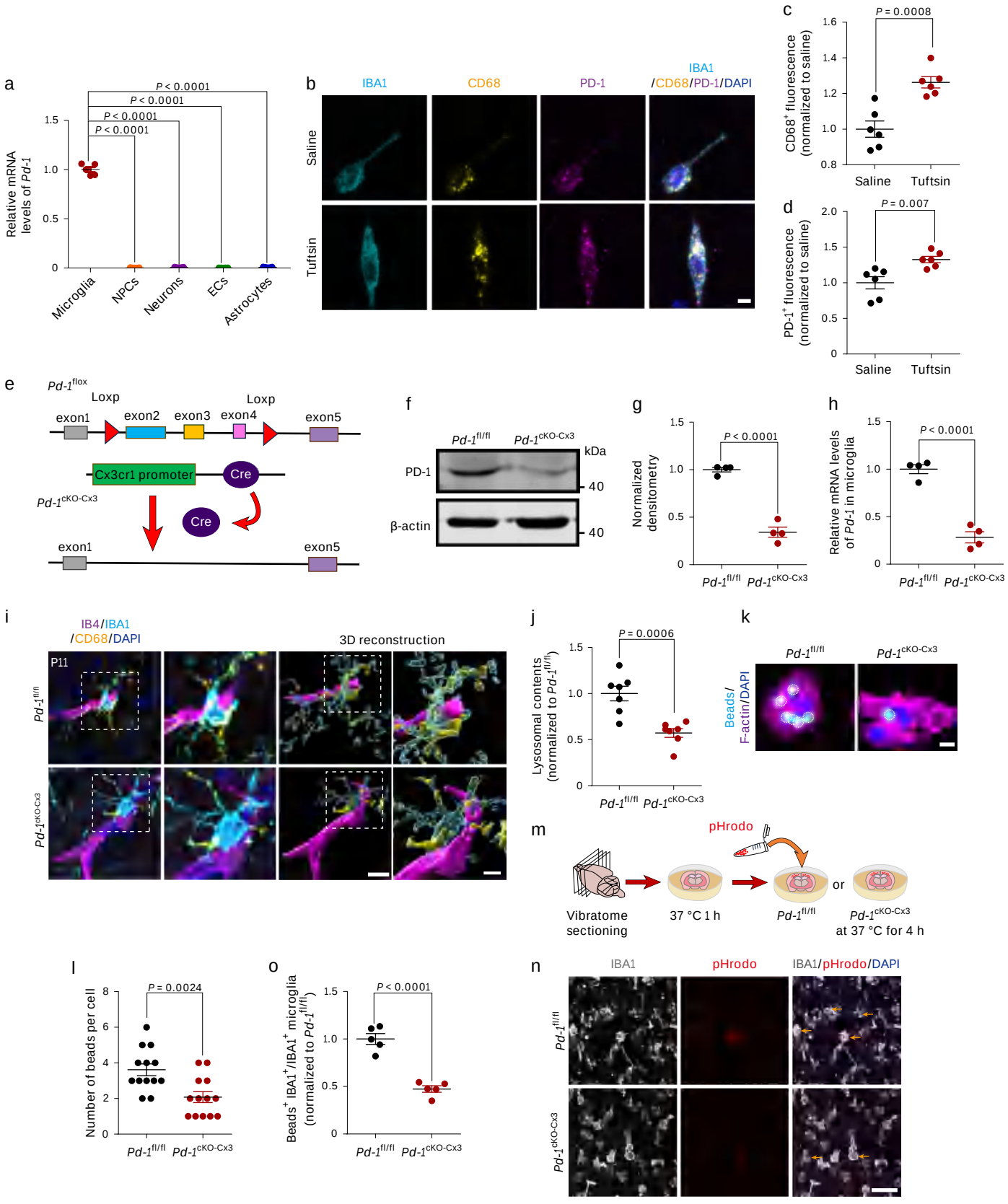

https://doi.org/10.1038/s41593-026-02378-x

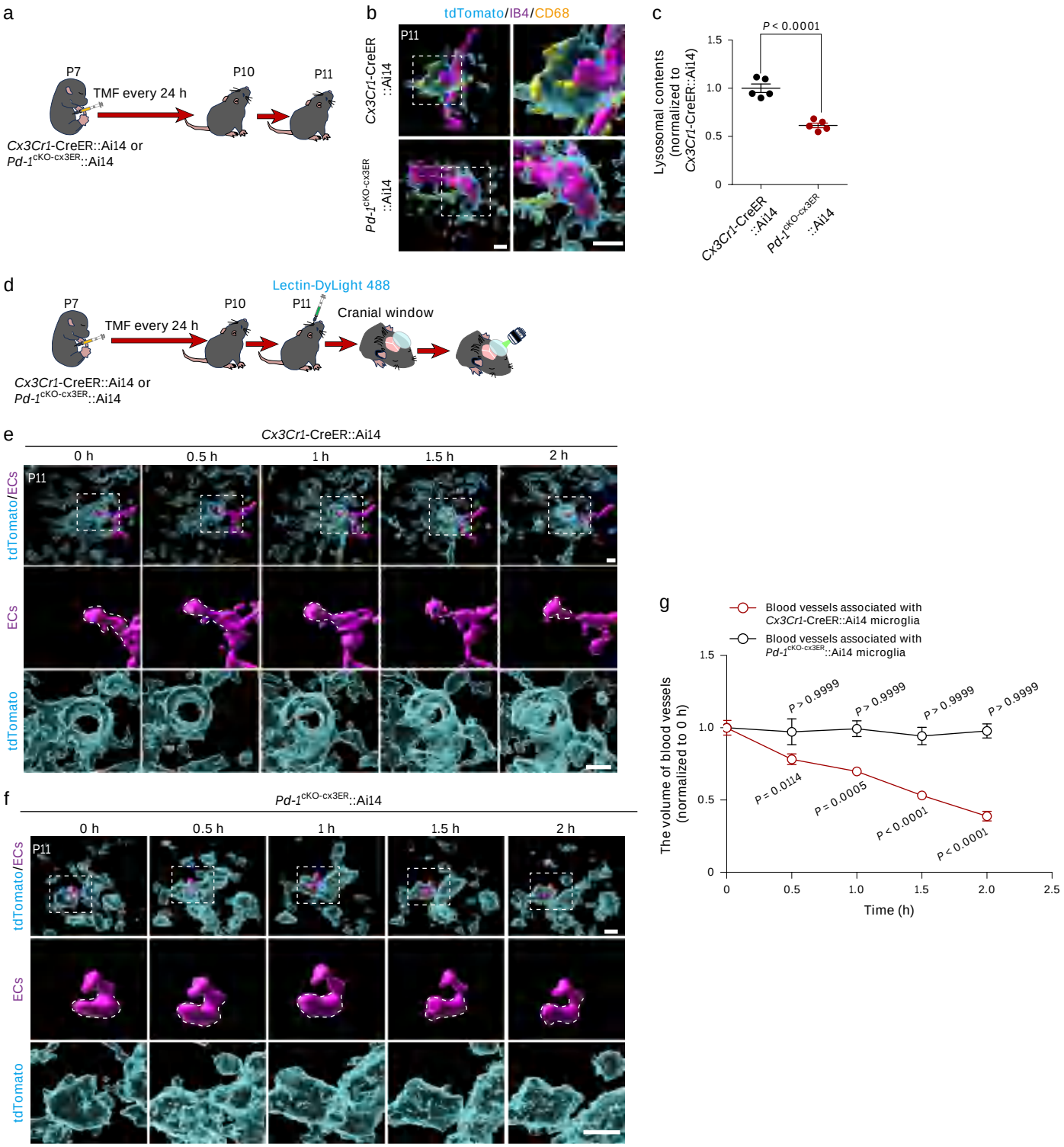

Fig. 4 | Deletion of PD-1 disrupts the paracrine pruning of cerebral vessels by microglia. a, *Cx3Cr1*-CreER::Ai14 or *Pd-1*$^{cKO\text{-}cx3ER}$::Ai14 mice at P7 were intraperitoneally injected with tamoxifen for 3 days, and then analyzed at P11. **b**, The 3D reconstruction of CD68^{+} lysosomes in *Cx3Cr1*-CreER::Ai14 and *Pd-1*$^{cKO\text{-}cx3ER}$::Ai14 microglia at P11. Scale bars, 5 µm. The right insets indicated higher magnification images of the delineated areas. Scale bars, 5 µm. **c**, Quantitative statistics of lysosomal content. $n = 5$ cells from five mice. **d**, *Cx3Cr1*-CreER::Ai14 or *Pd-1*$^{cKO\text{-}cx3ER}$::Ai14 mice were injected with tamoxifen intraperitoneally for 3 days at P7, then injected with Lectin-DyLight 488 intravenously at P11, and in vivo imaging were performed. **e**, Time-lapse images of cerebral vessels associated with microglia after intravenous injection of Lectin-DyLight 488 in *Cx3Cr1*- CreER::Ai14 mice at P11. Scale bars, 10 µm. **f**, Time-lapse images of cerebral vessels associated with microglia after intravenous injection of Lectin-DyLight 488 in *Pd-1*$^{cKO\text{-}cx3ER}$::Ai14 mice at P11. Scale bars, 10 µm. **g**, Quantification analysis of cerebral vascular volume associated with microglia in *Cx3Cr1*-CreER::Ai14 or *Pd-1*$^{cKO\text{-}cx3ER}$::Ai14 mice. $n = 5$ mice per group. For **c**, data were analyzed using a two-tailed unpaired *t*-test. For **g**, data were analyzed using a repeated-measures two-way ANOVA with Bonferroni's test. Data are presented as mean ± s.e.m. for **c** and **g**.

https://doi.org/10.1038/s41593-026-02378-x

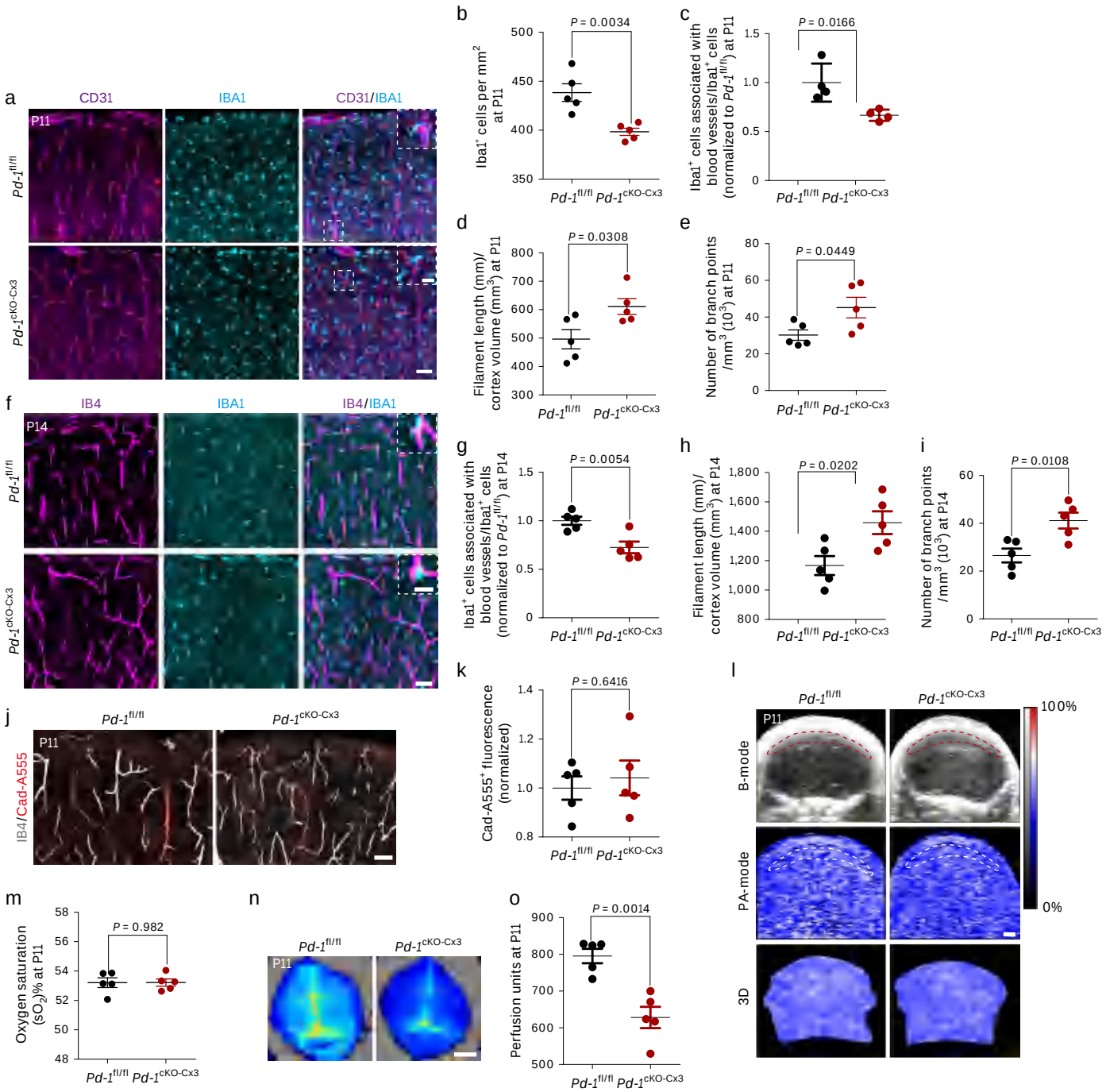

Fig. 5 | Abnormal paracrine pruning of cerebral vasculature by microglia resulting in excessive vascularization. a, Confocal immunofluorescence image of cerebral vessels (CD31, purple) and microglia (IBA1, blue) in *Pd-1*$^{fl/fl}$ and *Pd-1*$^{cKO\text{-}Cx3}$ brain cortex at P11. Scale bars, 50 µm (overview) and 20 µm (inset and rendering). **b**, Quantitative analysis of Iba1$^+$ cells in the mouse cerebral cortex at P11. $n = 5$ brain slices from four mice. **c**, Quantitative analysis of vessel-associated IBA1$^+$ cells in all IBA1$^+$ cells at P11. $n = 4$ brain slices from four mice. **d**,**e**, Quantification of the vessel length (**d**) and branch points (**e**) in the brain cortex. $n = 5$ brain slices from five mice. **f**, High-magnification confocal images of cerebral vessels (IB4, purple) and microglia (IBA1, blue) in *Pd-1*$^{fl/fl}$ and *Pd-1*$^{cKO\text{-}Cx3}$ brain cortex at P14. Scale bars, 50 µm (overview) and 5 µm (inset and rendering). **g**, Quantitative of vessel-associated IBA1$^+$ cells in all IBA1$^+$ cells at P14. $n = 5$ brain slices from five mice. **h**,**i**, Quantification of the filament length (**h**) and the number of branch points (**i**) in the brain cortex at P14. $n = 5$ brain slices from five mice. **j**, Confocal images of IB4 and Cad-A555 showed no cadaverine extravasation in *Pd-1*$^{fl/fl}$ and *Pd-1*$^{cKO\text{-}Cx3}$ blood vessels at P11. **k**, Quantitative analysis of extravascular leakage. $n = 5$ mice per group. **l**, Ultrasonograms and 2D and 3D photoacoustic (PA) functional images of brain sO_2 in *Pd-1*$^{fl/fl}$ and *Pd-1*$^{cKO\text{-}Cx3}$ brain cortex at P11. The dashed area represents the cerebral cortex. Scale bars, 1 mm. **m**, Representative images showed that sO_2 levels remain unchanged in *Pd-1*$^{cKO\text{-}Cx3}$ cerebral blood vessels. $n = 5$ mice per group. **n**, Laser speckle contrast imaging system was used to monitor the blood perfusion in *Pd-1*$^{fl/fl}$ and *Pd-1*$^{cKO\text{-}Cx3}$ mice at P11. Scale bars, 3 mm. **o**, Blood perfusion decreased after *Pd-1* deficiency in microglia at P11. $n = 5$ mice per group. Scale bars, 50 µm. For **b**–**e**,**g**–**i**,**k**,**m**,**o**, data were analyzed using a two-tailed unpaired *t*-test. Data are presented as mean ± s.e.m. for **b**–**e**,**g**–**i**,**k**,**m**,**o**.

and vessel-associated IBA1$^+$ cells in *Pd-1*$^{cKO\text{-}Cx3}$ mice, accompanied by increased cerebral vessel length and branch point number (Fig. 5b–e). These findings were corroborated by IB4 immunofluorescence staining at P11 (Extended Data Fig. 6a–f). We next explored a late stage of vascular remodeling (P14). Immunofluorescence staining revealed sustained reductions in vessel-associated IBA1$^+$ cells and increased cerebral vessel length and branch point number in *Pd-1*$^{cKO\text{-}Cx3}$ brain cortex at P14, indicating that PD-1-dependent microglial pruning of cerebral vessels is persistent during vascular development (Fig. 5f–i). Meanwhile, we examined the changes in microglia and cerebral vessels after *Pd-1* deficiency at P20 and P40. The results showed that microglia and cerebral vessels were unchanged after weaning and adulthood in mice, suggesting that *Pd-1* lost its regulatory function on microglia (Extended Data Fig. 6g–p).

Next, we observed that the tight junctions of *Pd-1*$^{cKO\text{-}Cx3}$ cerebral vessels were not altered compared to those in *Pd-1*$^{fl/fl}$ (Extended Data Fig. 7a–e). To assess whether microglia abnormalities disrupt blood–brain barrier integrity, we used the fluorescent tracer Alexa Fluor 555 cadaverine (Cad-A555). No cadaverine leakage was detected in the *Pd-1*$^{fl/fl}$ and *Pd-1*$^{cKO\text{-}Cx3}$ vasculature (Fig. 5j,k). Moreover, to determine if the abnormal increase in cerebral vasculature resulted from altered proliferation or apoptosis, we performed Ki67 and TUNEL immunofluorescence staining. Results showed that *Pd-1*-deficient microglia did not affect cerebrovascular proliferation or apoptosis (Extended Data Fig. 7f–k). Subsequently, we dynamically monitored oxygen saturation (sO_2) levels in mouse cerebral vessels using in vivo photoacoustic imaging systems, which combine the high-sensitivity optical imaging and the high-resolution ultrasonography. Ultrasonograms and two-dimensional (2D)/3D photoacoustic functional images showed that sO_2 was similar in the *Pd-1*$^{fl/fl}$ and *Pd-1*$^{cKO\text{-}Cx3}$ cerebral vasculature at P11, P20 and P40 (Fig. 5l,m and Extended Data Fig. 7l,m). Previous studies have shown that the loss of microglia affects vasodilative response, leading to abnormal cerebral blood flow[23–25]. We therefore detected cerebral blood flow through the laser speckle contrast imaging system in *Pd-1*$^{fl/fl}$ and *Pd-1*$^{cKO\text{-}Cx3}$ mice. The results showed that blood perfusion was reduced in *Pd-1*$^{cKO\text{-}Cx3}$ cerebral vasculature at P11, but this change disappeared after weaning (Fig. 5n,o and Extended Data Fig. 7n,o). To investigate microglia-ECs crosstalk, we isolated primary brain ECs and co-cultured them with microglia from *Pd-1*$^{fl/fl}$ or *Pd-1*$^{cKO\text{-}Cx3}$ cerebral cortex using Transwell membranes (Extended Data Fig. 7p). The results showed that the proliferation of ECs was also not affected, suggesting that microglia and ECs interacted through direct contact (Extended Data Fig. 7q–s). Together, these results suggested that microglia play an important role in early brain vascular development.

PD-1 guides microglia to prune cerebral vasculature through CD5L secretion

To explore downstream targets of PD-1, we isolated CD45$^+$CD11b$^+$ cells from *Pd-1*$^{fl/fl}$ and *Pd-1*$^{cKO\text{-}Cx3}$ cerebral cortex at P11 by flow cytometry and sequenced the RNA transcriptome (Extended Data Fig. 8a,b). Flow-sorting data showed that the number of CD45$^+$CD11b$^+$ cells was reduced in *Pd-1*$^{cKO\text{-}Cx3}$ cerebral cortex (Extended Data Fig. 8c). According to Gene Ontology (GO) analysis, the downregulated and the upregulated genes were enriched in terms related to autophagy and cell adhesion molecule binding (Fig. 6a,b). The heatmap and volcano plots revealed altered gene expression profiles in *Pd-1*$^{cKO\text{-}Cx3}$ microglia, with 3,021 upregulated genes and 2,736 downregulated genes (Extended Data Fig. 8d,e). Subsequently, we screened ten secreted proteins with high different expressions, and the results showed that CD5L was downregulated most obviously, which was consistent with the results of qPCR (Fig. 6c,d). CD5L is expressed and secreted primarily by macrophages and is emerging as an important immune effector. Also, CD5L serves as a marker for phagocytes, enabling them to efficiently recognize and phagocytose substances[26,27]. Therefore, we detected expression of CD5L in different cells and qPCR showed that CD5L was mostly expressed by microglia in the brain (Fig. 6e). Immunofluorescence staining revealed widespread CD5L expression in isolated primary microglia (Fig. 6f). ELISA demonstrated that CD5L was markedly reduced in *Pd-1*-deficient microglia, consistent with western blotting results (Fig. 6g and Extended Data Fig. 8f,g). To directly investigate the role of CD5L in microglia, we generated a mouse strain carrying a conditional knockout allele of *Cd5l* through targeted deletion of exon 3 to exon 5 (*Cd5l*$^{fl/fl}$). Next, we crossed *Cd5l*$^{fl/fl}$ mice with *Cx3cr1*-Cre mice to specifically abate *Cd5l* function in microglia (Fig. 6h). 3D reconstruction showed that the content of CD68$^+$ lysosomes in IBA1$^+$ cells was markedly reduced after CD5L deficiency (Fig. 6i,j). Concurrently, immunofluorescence staining showed that CD5L deficiency increased both the length and number of branch points of cerebral blood vessels (Fig. 6k–m). These results were consistent with the results of *Pd-1* deficiency in microglia.

Previous studies have reported CD36 as the primary cell surface receptor for CD5L, which induces macrophage autophagy to maintain cellular homeostasis, and it is expressed in many cell types, such as vascular ECs, phagocytes and specialized epithelial cells[28,29]. In vitro and in vivo results showed that CD36 was co-labeled with cerebral vessels (Extended Data Fig. 8h,i). To validate whether CD5L targets cerebral vessels via interaction with CD36, we performed co-immunoprecipitation (Co-IP) experiments. Results showed that HA-tagged CD36 could pull down exogenous CD5L in ECs, indicating a direct interaction between CD5L and CD36 (Fig. 6n). To explore the molecular signaling mechanisms of microglia on cerebral vascular pruning, we performed the Kyoto Encyclopedia of Genes and Genomes analysis on the RNA sequencing dataset and found potential responses involving MAPK signaling pathway (Extended Data Fig. 9a). Western blotting showed that p-Erk1/2 and p-mTOR were markedly increased in *Pd-1*$^{cKO\text{-}Cx3}$ microglia (Extended Data Fig. 9b,c). Previous studies have shown that PD-1 suppresses macrophage function by recruiting SHP-1/SHP-2 to its tail domain[30]. Meanwhile, PD-L1 affects neuron function through PD-1 and downstream tyrosine phosphatase SHP-1 (refs. 12,31). Treatment of primary microglia with the SHP-1 inhibitor TPI-1 increased p-Erk1/2 and p-mTOR levels, suggesting PD-1 regulates the Erk1/2–mTOR signaling pathway through SHP-1 (Extended Data Fig. 9d,e). Moreover, Rapamycin, an inhibitor of mTOR, rescued autophagy defects in IBA1$^+$ cells induced by *Pd-1* deficiency (Extended Data Fig. 9f,g). Collectively, these results suggest that the PD-L1–PD-1 axis directs microglia to secrete CD5L through the Erk1/2–mTOR signaling pathway, and that microglia-derived CD5L interacts with the CD36 receptor to influence cerebral vascular remodeling.

Exogenous CD5L promotes microglial function for cerebrovascular pruning

To determine whether CD5L is necessary for microglia phagocytosis, we injected CD5L protein intracerebroventricularly at P11 and collected brain tissue 4 h later (Fig. 7a). CD5L levels were markedly elevated at the injection site (Extended Data Fig. 10a,b). Immunostaining revealed that exogenous CD5L increased the number of IBA1$^+$ cells associated with blood vessels (Fig. 7b,c). Moreover, the lysosomal marker CD68 of IBA1$^+$ cells also increased markedly after CD5L protein injection, indicating that CD5L restores phagocytic activity impaired by PD-1 deficiency (Fig. 7d,e). We next co-cultured primary microglia with green fluorescent beads in vitro. The addition of CD5L protein enhanced microglial phagocytosis, corroborating our in vivo findings (Fig. 7f,g). To further assess the effect of CD5L on microglia, we transduced primary microglia with lentivirus for about 24 h and immunofluorescence staining showed that the percentage of GFP$^+$IBA1$^+$/IBA1$^+$ reached 80% (Extended Data Fig. 10c,d). Notably, CD68 fluorescence in *Pd-1*$^{cKO\text{-}Cx3}$ IBA1$^+$cells overexpressing *Cd5l* was comparable to that in *Pd-1*$^{fl/fl}$ IBA1$^+$ cells (Fig. 7h,i). Exogenous CD5L also rescued the changes of Erk1/2–mTOR signaling pathway in *Pd-1*$^{cKO\text{-}Cx3}$ microglia

https://doi.org/10.1038/s41593-026-02378-x

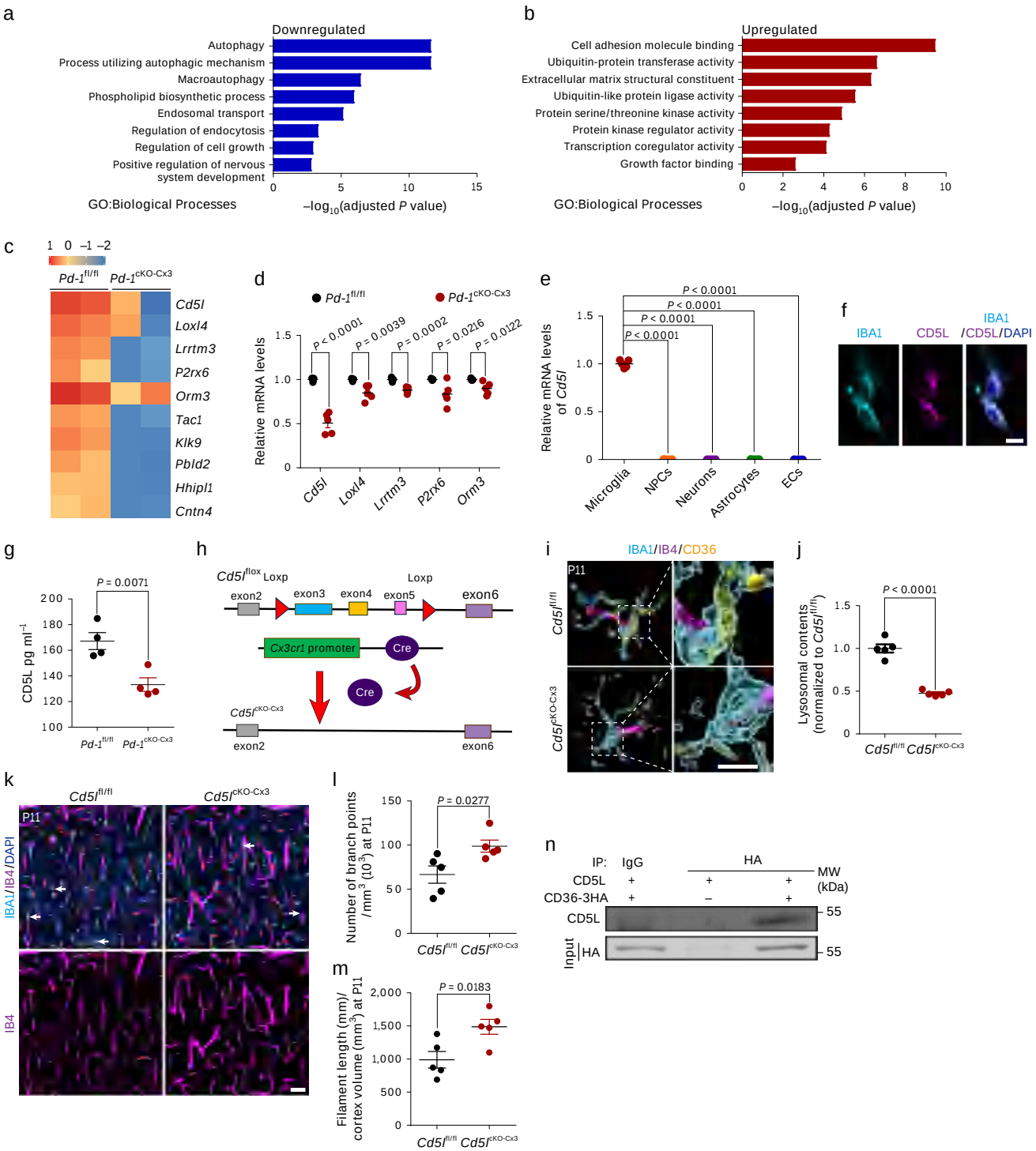

Fig. 6 | Microglia assist in sculpting cerebral vessels through CD5L–CD36 coupling. a,**b**, GO analysis of biological processes about the downregulated (**a**) and upregulated (**b**) genes in the microglia of *Pd-1*$^{cKO\text{-}Cx3}$ mice at P11. **c**, Heatmaps showed that *Cd5l* was one of the markedly differentially expressed genes. **d**, qPCR was performed for five genes that were significantly expressed in the microglia of *Pd-1*$^{fl/fl}$ and *Pd-1*$^{cKO\text{-}Cx3}$ mice. $n = 5$ mice per group. **e**, The relative mRNA levels of *Cd5l* in microglia, neural progenitor cells (NPCs), neurons, astrocytes and ECs. *Gapdh* was an internal reference gene. $n = 5$ mice per group. **f**, Representative confocal images showed that IBA1 was co-labeled with CD5L. Scale bars, 10 μm. These results were independently repeated in three separate experiments from three mice, and consistent findings were obtained. **g**, CD5L protein from the cultured microglia was measured by an ELISA kit. $n = 4$ mice per group. **h**, Schematic diagram of conditional deletion of *Cd5l* in microglia. **i**, 3D reconstruction of the interaction between microglia and brain blood vessels in *Cd5l*$^{fl/fl}$ and *Cd5l*$^{cKO\text{-}Cx3}$ mice brain at P11. Scale bars, 5 μm. **j**, Quantitative analysis showed reduced CD68$^+$ lysosome content in *Cd5l*$^{cKO\text{-}Cx3}$ microglia. $n = 5$ cells from five mice. **k**, Confocal immunofluorescence images of cerebral vessels and microglia in *Cd5l*$^{fl/fl}$ and *Cd5l*$^{cKO\text{-}Cx3}$ brain cortex at P11. Scale bars, 50 μm. **l**,**m**, Quantitative analysis of the branch points (**l**) and vessel length (**m**) in the *Cd5l*$^{fl/fl}$ and *Cd5l*$^{cKO\text{-}Cx3}$ brain cortex. $n = 5$ brain slices from five mice. **n**, Co-IP experiments were used to verify the interaction between CD5L and CD36 in ECs. These results were independently repeated in three separate experiments, and consistent findings were obtained. For **a** and **b** were analyzed using a two-tailed modified Fisher's exact test with Benjamini–Hochberg correction. For **d**,**g**,**j**,**l**,**m**, data were analyzed using a two-tailed unpaired *t*-test. For **e**, data were analyzed using a one-way ANOVA with Dunnett's test. Data are presented as mean ± s.e.m. for **d**,**e**,**g**,**j**,**l**,**m**.

https://doi.org/10.1038/s41593-026-02378-x

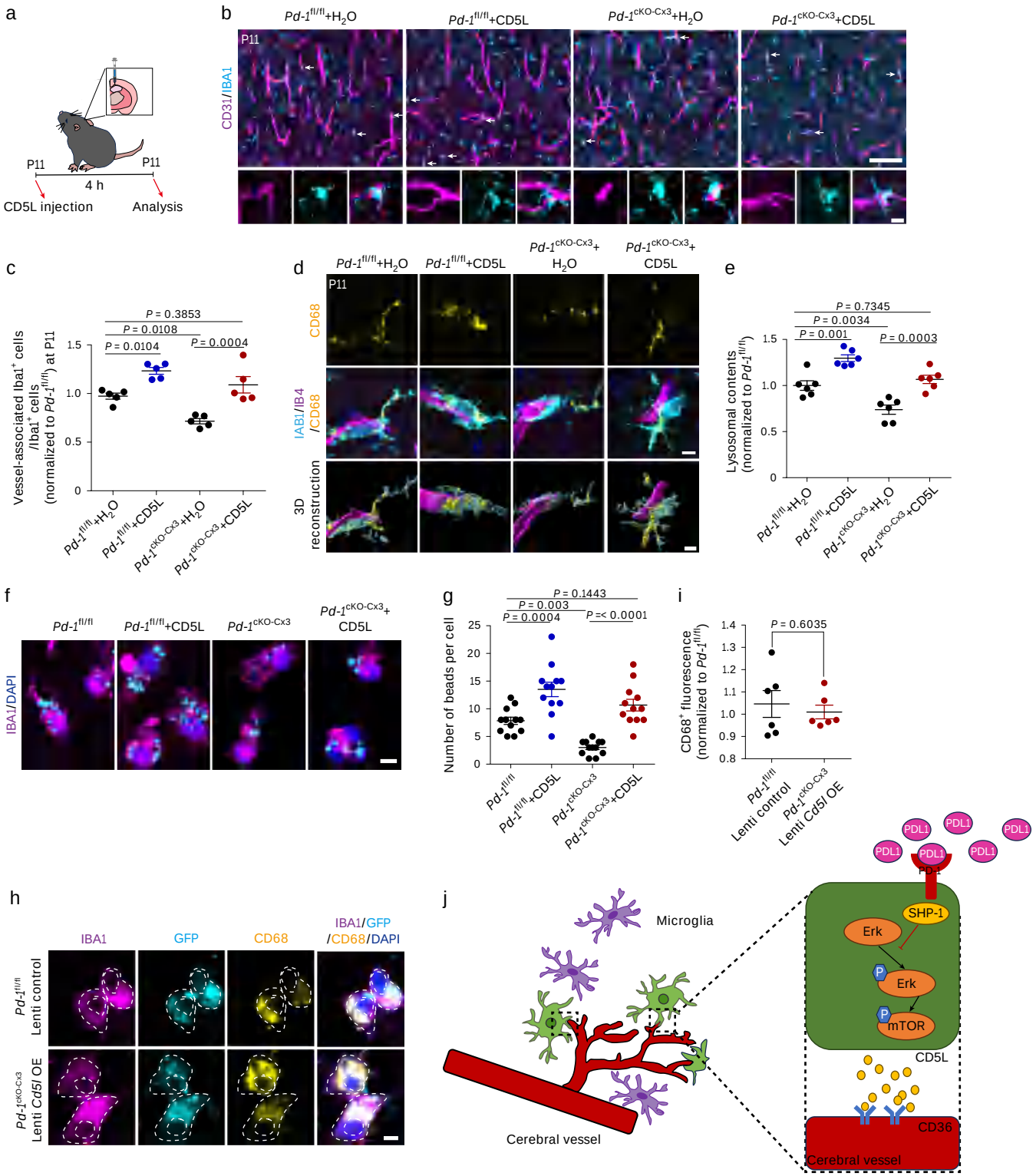

Fig. 7 | CD5L rescues abnormal cerebrovascular pruning by microglia deficient in PD-1. a, Scheme illustrated CD5L protein was injected into *Pd-1*$^{fl/fl}$ or *Pd-1*$^{cKO\text{-}Cx3}$ mice at P11, tissues were collected and analyzed after 4 h. Mice brain ventricles were injected with equal volume of water as control group. **b**, Representative images of cerebral vessels (CD31, purple) and microglia (IBA1, blue) in *Pd-1*$^{fl/fl}$ and *Pd-1*$^{cKO\text{-}Cx3}$ brain cortex after injection of CD5L protein at P11. Scale bars, 100 μm (overview) and 10 μm (inset and rendering). **c**, Quantitative analysis of vessel-associated Iba1$^+$ cells in all Iba1$^+$ cells after injection of CD5L protein in *Pd-1*$^{fl/fl}$ and *Pd-1*$^{cKO\text{-}Cx3}$ mice. $n = 5$ brain slices from five mice. **d**, Representative images and 3D render of microglia containing lysosomes in CD5L-injected mice at P11. Scale bars, 5 μm. **e**, Quantitative of microglia lysosomal contents in CD5L-injected mice. $n = 6$ cells from six mice. **f**, Primary microglial were incubated with fluorescent microbeads (blue) and CD5L protein for 4 h. Scale bars, 5 μm. **g**, Quantitative analysis of primary cortical microglia phagocytosis experiments after adding CD5L protein. $n = 12$ cells from six mice. **h**, Immunostaining for IBA1 and CD68 in primary microglia transfected with PCDH-3Flag-GFP or PCDH-3Flag-GFP-*Cd5l*. Scale bars, 5 μm. **i**, Quantitative of CD68$^+$ fluorescence. $n = 6$ cells from six mice. **j**, The model of PD-1 directing microglia phagocytosis to prune brain vessels. For **c**,**e**,**g**, data were analyzed using a one-way ANOVA with Tukey's test. For **i**, data were analyzed using two-tailed unpaired *t*-test. Data are presented as mean ± s.e.m. for **c**,**e**,**g**,**i**.

(Extended Data Fig. 10e,f). In summary, our study elucidated insights of the important relationship between microglia and cerebral vascular reconstruction. PD-1 drives microglia to secrete CD5L, thereby contributing to cerebral vascular pruning (Fig. 7j).

Discussion

The cerebrovascular system comprises highly branched vascular networks that are precisely adapted to support the complex functional demands of the brain. The cerebrovascular system not only experienced angiogenesis, but also underwent extensive vascular pruning, which transformed the initial exuberant interconnected meshwork into a simplified architecture[32–34]. Microglia, the resident macrophages of the brain parenchyma, are critical regulators of neural circuit refinement owing to their high motility and phagocytic capacity[35,36]. Although recent research has largely focused on the role of microglial phagocytosis in neural circuit remodeling, its contribution to cerebrovascular pruning has received less attention[37–39]. Here, we demonstrate that microglia participate in cerebrovascular pruning to facilitate the formation of a simplified vascular network. PD-1 deficiency reduced the VAM presence and impaired their pruning activity, resulting in abnormal vascular morphology. Our findings reveal a previously unrecognized role for vascular-associated microglia in mediating vessel pruning during cerebrovascular remodeling.

During cerebrovascular development, vessels initially form through sprouting angiogenesis and subsequently undergo extensive remodeling to achieve a mature, functional architecture[40]. This remodeling involves the pruning of vascular segments, which has been attributed to EC migration, redeployment and apoptosis[41,42]. Here, we identified a subset of microglia that intimately associate with cerebral vasculature. These VAM exhibited high expression of the lysosomal marker CD68, suggesting strong phagocytic potential. This interaction peaked around P11, indicating a critical period for microglia–vessel interaction. As in vitro conditions poorly recapitulate the native microglial state, we employed in vivo live imaging to dynamically monitor these interactions[43]. We observed microglia extending active pseudopodia toward smaller-diameter vessels, subsequently enwrapping them. Subsequently, the volume of microglia-associated vessels gradually decreased until they disappeared; however, not all VAM perform pruning function. We found that approximately half of the microglia leave the cerebral blood vessels within 2 h.

PD-1 is an immune checkpoint regulator that plays a key role in suppressing immune responses and promoting self-tolerance[9,44]. Microglia, as the principal immune effector cells in the CNS, act as first responders to homeostatic and pathological changes, similar to peripheral immune cells[45–47]. Like macrophages, T cells and B cells, microglia continuously monitor their microenvironment and neighboring cells, clearing cellular debris and metabolites while facilitating intercellular communication[48]. Consistent with previous results, we observed high PD-1 expression in CNS microglia, which was further upregulated following activation with the microglial agonist Tuftsin[14].

Through in vivo and in vitro experiments, we found that *Pd-1* deficiency impacted both the abundance and phagocytic capacity of microglia. These findings suggest that PD-1 may influence cerebrovascular pruning through two potential mechanisms: (1) direct regulation of microglia-mediated pruning activity, and (2) indirect reduction of pruning capacity by decreasing microglial numbers. Previous microglia-depletion studies have shown that vascular function is compromised but can be restored upon microglial repopulation[23–25]. In our experiments, defective microglial pruning led to increased vascular density yet reduced cerebral blood flow. Notably, PD-1 dependent regulation of vascular pruning was restricted to the early postnatal period and declined after weaning, consistent with the known timeline of active cerebrovascular remodeling. PD-L1 and PD-L2 are established endogenous ligands of PD-1. Both in vivo and in vitro data indicated that modulating PD-L1 levels affected microglial phagocytosis, supporting a role for the PD-L1–PD-1 axis in this process. Using mouse brain slice preparations, we found that conditional knockout of PD-1 in microglia did not affect the release of PD-L1 and PD-L2 in the brain (Extended Data Fig. 3g–i). Subsequently, via loss-of-function (treatment with anti-PD-L1 antibody) and gain-of-function (exogenous PD-L1 treatment) approaches, we discovered that loss of PD-L1 in microglia led to abnormal increases in cerebral vasculature, while exogenous PD-L1 supplementation enhanced the number of vasculature-associated microglia (Extended Data Fig. 4d–m). These findings suggest that the PD-L1–PD-1 signaling axis is essential for microglia-dependent cerebrovascular pruning during early neurodevelopment. Previous studies have demonstrated that the inhibition of the PD-1 pathway promotes immune-mediated clearance of cerebral β-amyloid plaques and rescues memory deficits in AD[49,50]. Additionally, blockade of the PD-L1–PD-1 pathway has been shown to facilitate the elimination of senescent cells[51]. Together, these findings suggest that a potential benefit of PD-L1–PD-1 signal inhibition. In contrast, we found that inhibiting this pathway impairs microglial phagocytosis, leading to an increase in abnormal cerebral vasculature. Due to the marked context-dependence and spatiotemporal heterogeneity of microglia[52], we hypothesize that the PD-L1–PD-1 signaling axis may exert divergent regulatory functions in microglia depending on their state. Although inhibiting this pathway under aging or disease conditions could be beneficial, its role during early postnatal development remains to be fully elucidated. Furthermore, we found that PD-1 expression is highest in microglia compared to other cell types in the brain (Fig. 3a); however, recent single-cell and spatial transcriptomic studies of AD have shown that in protective microglial states, PD-L1 expression is markedly upregulated, accompanied by reduced inflammatory cytokine levels and enhanced phagocytic activity. Moreover, abnormal activation of PD-L1 signaling has also been detected in innate immune cells, including disease-associated microglia, in the brains of patients with AD. These observations indicate that, similar to PD-1, PD-L1 may also play a key regulatory role in microglial function[53,54].

Subsequently, combined with RNA sequencing results, we screened for a downstream secreted factor CD5L, which could be used as a 'search and destroy' weapon. Previous studies have shown that CD5L released from macrophages circulates throughout the body, and when CD5L is engulfed by phagocytes, substances bound to CD5L are also phagocytosed, thus achieving the function of clearance[55,56].

Microglia exercise physical surveillance of the microenvironment through ligand–receptor interactions. Previous studies have demonstrated that the scavenger receptor CD36 may serve as a cellular receptor for CD5L endocytosis[28]. In agreement with this, our Co-IP assays confirmed a direct interaction between CD5L and CD36. Given the established role of the mTOR signaling pathway in regulating diverse cellular processes, including cell growth, metabolism and phagocytosis[57]. We investigated its involvement in microglial function. Our data indicate that microglia modulate phagocytic activity through the Erk1/2–mTOR signaling axis. Of note, both in vivo and in vitro experiments showed that exogenous CD5L protein rescues the phagocytic defects resulting from *Pd-1* deficiency. Together, our findings reveal a previously unknown role for microglia in shaping an efficient cerebral vascular network through participation in cerebrovascular pruning. Meanwhile, we found that PD-1 directs microglia to cerebral blood vessels via CD5L secretion, thereby enabling specific microglia–vessel interactions.

Limitations of the study

In this study, through in vivo imaging, we observed that some microglia tend to enwrap cerebral vessels. At the same time, we also observed that not all VAM perform auxiliary pruning functions, and half of them leave cerebral vessels spontaneously; however, due to the technical challenge of isolating these specific VAM, we could not definitively characterize

the subpopulation responsible for vascular pruning. It also remains unclear whether *Pd-1* expression differs between pruning-competent microglia and other microglial subsets. Because immunofluorescence provides only static snapshots, our analysis was limited to the collective state of all VAM. Future studies will require new methodologies to dynamically track and molecularly profile this functionally distinct subset. Furthermore, previous studies have demonstrated that microglial pruning of neuronal synapses may not solely result from phagocytosis but can also occur through alternative modalities[58]. For instance, neurons can undergo activity-dependent synaptic elimination autonomously, with microglia acting more as subsequent 'clearers' rather than initiators of synaptic removal. Therefore, the 'pruning' of blood vessels by microglia observed in our study does not necessarily imply a phagocytic mechanism, but may instead be mediated by other pathways, which warrants investigation in future research.

For cerebral vessels, we found that smaller-diameter cerebral vessels recruit microglia to associate with them, but not all the associated cerebral vessels were pruned by microglia. The specific mechanism by which cerebral blood vessels recruit microglia for selective pruning requires further study. Meanwhile, although our Co-IP experiments demonstrated that CD5L binds to endothelial CD36, we have not explored the specific function of endothelial CD36 (for instance, whether endothelial-specific knockout of CD36 also affects microglial targeting of cerebral blood vessels). These questions require further investigation in subsequent studies. Additionally, we found that PD-1 deficiency not only affected the phagocytosis of microglia, but also impaired their autophagy. Therefore, the autophagy process of cerebral vessels in microglia lysosomes needs to be further explored.

Online content

Any methods, additional references, Nature Portfolio reporting summaries, source data, extended data, supplementary information, acknowledgements, peer review information; details of author contributions and competing interests; and statements of data and code availability are available at https://doi.org/10.1038/s41593-026-02378-x.

References

1. Sato, K. Effects of microglia on neurogenesis. *Glia* **63**, 1394–1405 (2015).
2. Hughes, A. N. & Appel, B. Microglia phagocytose myelin sheaths to modify developmental myelination. *Nat. Neurosci.* **23**, 1055–1066 (2020).
3. Kisler, K., Nikolakopoulou, A. M. & Zlokovic, B. V. Microglia have a grip on brain microvasculature. *Nat. Commun.* **12**, 5290 (2021).
4. Denes, A. et al. Endothelial cells and macrophages as allies in the healthy and diseased brain. *Acta Neuropathol.* **147**, 38 (2024).
5. Mondo, E. et al. A developmental analysis of juxtavascular microglia dynamics and interactions with the vasculature. *J. Neurosci.* **40**, 6503–6521 (2020).
6. Grossmann, R. et al. Juxtavascular microglia migrate along brain microvessels following activation during early postnatal development. *Glia* **37**, 229–240 (2002).
7. Gordon, S. R. et al. PD-1 expression by tumour-associated macrophages inhibits phagocytosis and tumour immunity. *Nature* **545**, 495–499 (2017).
8. Nishimura, H., Nose, M., Hiai, H., Minato, N. & Honjo, T. Development of lupus-like autoimmune diseases by disruption of the PD-1 gene encoding an ITIM motif-carrying immunoreceptor. *Immunity* **11**, 141–151 (1999).
9. Zhao, J., Roberts, A., Wang, Z., Savage, J. & Ji, R. R. Emerging role of PD-1 in the central nervous system and brain diseases. *Neurosci. Bull.* **37**, 1188–1202 (2021).
10. Zhao, J. et al. PD-L1/PD-1 checkpoint pathway regulates hippocampal neuronal excitability and learning and memory behavior. *Neuron* **111**, 2709–2726.e2709 (2023).
11. Zhao, S., Li, F., Leak, R. K., Chen, J. & Hu, X. Regulation of neuroinflammation through programed death-1/programed death ligand signaling in neurological disorders. *Fronti. Cell. Neurosci.* **8**, 271 (2014).
12. Chen, G. et al. PD-L1 inhibits acute and chronic pain by suppressing nociceptive neuron activity via PD-1. *Nat. Neurosci.* **20**, 917–926 (2017).
13. Filippone, A. et al. PD1/PD-L1 immune checkpoint as a potential target for preventing brain tumor progression. *Cancer Immunol. Immunother.* **71**, 2067–2075 (2022).
14. Kummer, M. P. et al. Microglial PD-1 stimulation by astrocytic PD-L1 suppresses neuroinflammation and Alzheimer's disease pathology. *EMBO J.* **40**, e108662 (2021).
15. Mecca, C., Giambanco, I., Donato, R. & Arcuri, C. Microglia and aging: the role of the TREM2-DAP12 and CX3CL1–CX3CR1 axes. *Int. J. Mol. Sci.* https://doi.org/10.3390/ijms19010318 (2018).
16. Yasuda, M., Nagappan-Chettiar, S., Johnson-Venkatesh, E. M. & Umemori, H. An activity-dependent determinant of synapse elimination in the mammalian brain. *Neuron* **109**, 1333–1349.e1336 (2021).
17. Coelho-Santos, V. & Shih, A. Y. Postnatal development of cerebrovascular structure and the neurogliovascular unit. *Wiley Interdiscip. Rev. Dev. Biol.* **9**, e363 (2020).
18. Jung, S. et al. Analysis of fractalkine receptor CX(3)CR1 function by targeted deletion and green fluorescent protein reporter gene insertion. *Mol. Cell. Biol.* **20**, 4106–4114 (2000).
19. Barca, C. et al. The colony stimulating factor-1 receptor (CSF-1R)-mediated regulation of microglia/macrophages as a target for neurological disorders (glioma, stroke). *Front. Immunol.* **12**, 787307 (2021).
20. Ren, X., Akiyoshi, K., Vandenbark, A. A., Hurn, P. D. & Offner, H. Programmed death-1 pathway limits central nervous system inflammation and neurologic deficits in murine experimental stroke. *Stroke* **42**, 2578–2583 (2011).
21. Faust, T. E. et al. A comparative analysis of microglial inducible Cre lines. *Cell Rep.* **42**, 113031 (2023).
22. Miksa, M., Komura, H., Wu, R., Shah, K. G. & Wang, P. A novel method to determine the engulfment of apoptotic cells by macrophages using pHrodo succinimidyl ester. *J. Immunol. Methods* **342**, 71–77 (2009).
23. Császár, E. et al. Microglia modulate blood flow, neurovascular coupling, and hypoperfusion via purinergic actions. *J. Exp. Med.* https://doi.org/10.1084/jem.20211071 (2022).
24. Bisht, K. et al. Capillary-associated microglia regulate vascular structure and function through PANX1-P2RY12 coupling in mice. *Nat. Commun.* **12**, 5289 (2021).
25. Mills, S. A. et al. Fractalkine-induced microglial vasoregulation occurs within the retina and is altered early in diabetic retinopathy. *Proc. Natl Acad. Sci. USA* https://doi.org/10.1073/pnas.2112561118 (2021).
26. Sanchez-Moral, L. et al. Multifaceted roles of CD5L in infectious and sterile inflammation. *Int. J. Mol. Sci.* https://doi.org/10.3390/ijms22084076 (2021).
27. Sanjurjo, L., Aran, G., Roher, N., Valledor, A. F. & Sarrias, M. R. AIM/CD5L: a key protein in the control of immune homeostasis and inflammatory disease. *J. Leukocyte Biol.* **98**, 173–184 (2015).
28. Kurokawa, J. et al. Macrophage-derived AIM is endocytosed into adipocytes and decreases lipid droplets via inhibition of fatty acid synthase activity. *Cell Metab.* **11**, 479–492 (2010).
29. Silverstein, R. L. & Febbraio, M. CD36, a scavenger receptor involved in immunity, metabolism, angiogenesis, and behavior. *Sci. Signal.* **2**, re3 (2009).
30. Lorenz, U. SHP-1 and SHP-2 in T cells: two phosphatases functioning at many levels. *Immunol. Rev.* **228**, 342–359 (2009).

31. Jiang, C. et al. PD-1 Regulates GABAergic neurotransmission and GABA-mediated analgesia and anesthesia. *iScience* **23**, 101570 (2020).
32. Adams, R. H. & Alitalo, K. Molecular regulation of angiogenesis and lymphangiogenesis. *Nat. Rev. Mol. Cell Biol.* **8**, 464–478 (2007).
33. Potente, M., Gerhardt, H. & Carmeliet, P. Basic and therapeutic aspects of angiogenesis. *Cell* **146**, 873–887 (2011).
34. Ricard, N. & Simons, M. When it is better to regress: dynamics of vascular pruning. *PLoS Biol.* **13**, e1002148 (2015).
35. Nimmerjahn, A., Kirchhoff, F. & Helmchen, F. Resting microglial cells are highly dynamic surveillants of brain parenchyma in vivo. *Science* **308**, 1314–1318 (2005).
36. Favuzzi, E. et al. GABA-receptive microglia selectively sculpt developing inhibitory circuits. *Cell* **184**, 4048–4063.e4032 (2021).
37. Zhao, S., Umpierre, A. D. & Wu, L. J. Tuning neural circuits and behaviors by microglia in the adult brain. *Trends Neurosci.* **47**, 181–194 (2024).
38. Schalbetter, S. M. et al. Adolescence is a sensitive period for prefrontal microglia to act on cognitive development. *Sci. Adv.* **8**, eabi6672 (2022).
39. Weinhard, L. et al. Microglia remodel synapses by presynaptic trogocytosis and spine head filopodia induction. *Nat. Commun.* **9**, 1228 (2018).
40. Korn, C. & Augustin, H. G. Mechanisms of vessel pruning and regression. *Dev. Cell* **34**, 5–17 (2015).
41. Franco, C. A. et al. Dynamic endothelial cell rearrangements drive developmental vessel regression. *PLoS Biol.* **13**, e1002125 (2015).
42. Lenard, A. et al. Endothelial cell self-fusion during vascular pruning. *PLoS Biol.* **13**, e1002126 (2015).
43. Eme-Scolan, E. & Dando, S. J. Tools and approaches for studying microglia in vivo. *Front. Immunol.* **11**, 583647 (2020).
44. Boulanger, L. M. Immune proteins in brain development and synaptic plasticity. *Neuron* **64**, 93–109 (2009).
45. Caputa, G., Castoldi, A. & Pearce, E. J. Metabolic adaptations of tissue-resident immune cells. *Nat. Immunol.* **20**, 793–801 (2019).
46. Wang, A., Luan, H. H. & Medzhitov, R. An evolutionary perspective on immunometabolism. *Science* https://doi.org/10.1126/science.aar3932 (2019).
47. O'Neill, L. A. & Pearce, E. J. Immunometabolism governs dendritic cell and macrophage function. *J. Exp. Med.* **213**, 15–23 (2016).
48. Petry, P., Oschwald, A. & Kierdorf, K. Microglial tissue surveillance: the never-resting gardener in the developing and adult CNS. *Eur. J. Immunol.* **53**, e2250232 (2023).
49. Baruch, K. et al. PD-1 immune checkpoint blockade reduces pathology and improves memory in mouse models of Alzheimer's disease. *Nat. Med.* **22**, 135–137 (2016).
50. Chen, X. et al. Microglia-mediated T cell infiltration drives neurodegeneration in tauopathy. *Nature* **615**, 668–677 (2023).
51. Wang, T. W. et al. Blocking PD-L1-PD-1 improves senescence surveillance and ageing phenotypes. *Nature* **611**, 358–364 (2022).
52. Ardura-Fabregat, A. et al. Response of spatially defined microglia states with distinct chromatin accessibility in a mouse model of Alzheimer's disease. *Nat. Neurosci.* **28**, 1688–1703 (2025).
53. Ayata, P. et al. Lymphoid gene expression supports neuroprotective microglia function. *Nature* **648**, 157–165 (2025).
54. Gate, D. et al. Clonally expanded CD8 T cells patrol the cerebrospinal fluid in Alzheimer's disease. *Nature* **577**, 399–404 (2020).
55. Arai, S. et al. Apoptosis inhibitor of macrophage protein enhances intraluminal debris clearance and ameliorates acute kidney injury in mice. *Nat. Med.* **22**, 183–193 (2016).
56. Arai, S. & Miyazaki, T. A scavenging system against internal pathogens promoted by the circulating protein apoptosis inhibitor of macrophage (AIM). *Semin. Immunopathol.* **40**, 567–575 (2018).
57. Saxton, R. A. & Sabatini, D. M. mTOR signaling in growth, metabolism, and disease. *Cell* **169**, 361–371 (2017).
58. Eyo, U. & Molofsky, A. V. Defining microglial-synapse interactions. *Science* **381**, 1155–1156 (2023).

Methods

Plasmid constructs

To construct mammalian expression plasmids encoding *Cd5l* and *Cd36*, the coding sequences of mouse *Cd5l* (NM_009690.2) and mouse *Cd36* (NM_001159558.2) were amplified from mouse complementary DNA by PCR using PrimeSTAR Max DNA Polymerase (Takara, R045) with primers listed below. The PCR products were digested with *EcoRI* and *Not1*, followed by ligation into the similarly digested pCDH-3Flag vector (for *Cd5l*) and pCDH-3HA vector (for *Cd36*).

Cd5l-F: ATGGCTCCATTGTTCAACTTGATGCT
Cd5l-R: CTGATGTAACCACTGGGAGAATG
Cd36-F: ATGGGCTGTGATCGGAACTGTGG
Cd36-R: CATTTTGTAGATCGGCTTTACCA

Antibodies

The primary antibodies (supplier, cat. no. and dilution) used are listed as follows:

IB4 (Vector Labs, B-1205, AB_2314661, 1:1,000), CD68 (Bio-Rad, MCA1957GA, AB_324217, 1:1,000), IBA1 (Wako, 019-19741, AB_839504, 1:1,000), PD-1 (Abcam, ab214421, AB_2941806, 1:500), F-actin (CoraLite 594-conjugated phalloidin antibody, Proteintch, PF00003, 1:500), CD31 (BioLegend, 102406, AB_312901, 1:500), Ki67 (Abcam, ab15580, AB_443209, 1:1,000), CD5L (Abcam, ab45408, AB_726619, 1:500), HA (Cell Signaling Technology, 3724, AB_1549585, 1:1,000), mTOR (Cell Signaling Technology, 2972, AB_330978, 1:1,000), p-mTOR (Cell Signaling Technology, 5536S, AB_10691552, 1:1,000), Phospho-p44/42 MAPK (Erk1/2) (Cell Signaling Technology, 9101S, AB_331646, 1:1,000), p44/42 MAPK (Erk1/2) (Cell Signaling Technology, 9102, AB_330744, 1:1,000), ZO1 (Invitrogen, 40-2200, AB_2533456, 1:300), Claudin-5 (Invitrogen, 352500, AB_87321, 1:300), GFAP (Dako, Z0334, AB_10013382, 1:1,000), NeuN (Abcam, ab177487, AB_2532109, 1:1,000), CX3CR1 (Thermo Fisher Scientific, 14-6093-81, AB_467880, 1:1,000), Synapsin1 (Synaptic Systems, 106001, AB_2617071, 1:1,000), Homer1 (Synaptic Systems, 160003, AB_887730, 1:1,000), P62 (Proteintech, 18420-1-AP, AB_10694431, 1:1,000), LC3 (Proteintech, 14600-1-AP, AB_2137737, 1:1,000), BrdU (Abcam, AB6326, AB_305426, 1:1,000), CD36 (Novusbio, NB400-144, AB_920879, 1:300), GFP (MBL, D153-3, AB_591817, 1:1,000), anti-PD-L1 monoclonal antibody (BioX Cell, BE0101, AB_10949073, 1 μg) and anti-PD-L2 monoclonal antibody (BioX Cell, BE0112, AB_10950106, 1 μg).

The secondary antibodies were Alexa Fluor 488, Cy3 and Cy5 (Jackson ImmunoResearch).

Lentivirus production and infection

The lentiviral packaged plasmid (CD5L and CD36) and core plasmid were transfected into HEK293FT cells (ATCC, CRL-1573) by GenEscortI (Wisegen, WIS1100). The supernatant medium with lentivirus was collected at 24 h, 48 h and 72 h. Subsequently, the lentivirus was purified and centrifuged at 4500*g* for 40 min through a centrifugal concentrator (Millipore UFC9010). For microglia lentivirus infection, primary mouse microglia were treated with a mixture of lentivirus suspension containing CD5L plasmid and microglia culture medium containing 4 μg ml^{-1-1} Polybrene (Sigma, TR-1003-G) for 24 h, and then microglia were cultured for 24 h in new culture medium. For lentivirus infection of ECs, primary ECs were treated with a mixture of lentivirus suspension containing CD36 plasmid and ECs culture medium containing 4 μg ml^{-1} Polybrene for 24 h, and then ECs were cultured for 24 h in new culture medium.

Western blotting and co-immunoprecipitation

BCA assay was used to determine the protein concentration of the samples, which were lysed with RIPA buffer (Solarbio) containing 1% phenylmethyl sulfonyl fluoride (PMSF) and 1% Cocktail (Sigma). Subsequently, protein was separated by 12% SDS–PAGE gels and the protein bands were transferred to nitrocellulose (NC) membrane. The NC membrane was blocked in 5% de-fatted milk or bovine serum albumin (PBS + 0.05% Tween-20) at room temperature for 1 h, and were incubated with the primary antibodies overnight at 4 °C. Next day, the bands were incubated with secondary antibody at room temperature for 1 h, and then they were visualized by Odyssey (LI-COR Biosciences) software.

For co-immunoprecipitation, exogenous CD5L protein (1 μg ml^{-1}, MCE, HY-P72717) was added to ECs infected with PCDH-3HA (control) and CD36-3HA. Subsequently, cultured cells were lysed in lysis buffer (Beyotime Biotechnology) containing protease inhibitor cocktail and PMSF. Then, the fresh supernatants were incubated with anti-HA-tag (MBL, M132-11) in a rotating mixer at 4 °C overnight. The beads were washed with 0.02% PBST (Tween-20) three times, suspended in loading buffer and boiled for 5 min. The protein was analyzed by western blotting.

Immunostaining

Fluorescence immunostaining was performed as previously described. In brief, 40-μm brain sections were fixed with 4% paraformaldehyde (PFA) for 30 min, and then washed three times for 10 min with PBST (1% Triton X-100 in PBS). The brain sections were blocked with 5% bovine serum albumin for 1 h, and then incubated with primary antibodies at 4 °C overnight. Next day, the samples were incubated with fluorochrome-conjugated secondary antibodies at room temperature for 1 h. Finally, all brain sections were stained with DAPI (Sigma-Aldrich) for 5 min and visualized by microscopy (Zeiss LSM880).

qPCR

Total RNA was extracted from mouse cerebral cortex or cultured cells by using TRIzol (Invitrogen, 15596018) according to the manufacturer's instructions. cDNA was generated by the FastQuant RT kit (Tiangen, KR106-02) and qPCR assays were performed using the SYBR qPCR master mix (Tiangen) in an ABI7500 real-time PCR system (Applied Biosystems). The expression of β-actin was used as an endogenous control for normalization of qPCR reactions. For detecting the expression of *Pd-1* and *Cd5l* in different types of cells, *Gapdh* was used as an endogenous control to normalize qPCR. The qPCR primers for cDNA were as follows:

Cd31-F: TGGAAGTGTCCTCCCTTGAGC
Cd31-R: AAGGGAGCCTTCCGTTCTTAGG
Pd-1-F: TCCAACTGGTCGGAGGATCT
Pd-1-R: TGTATGATCTGGAAGCGGGC
Cdh5-F: ATTGGCCTGTGTTTTCGCAC
Cdh5-R: CACAGTGGGGTCATCTGCAT
Cx3cr1-F: AGTCAACATCCTGGGCTTCG
Cx3cr1-R: AGGATGAGTCTGACGGCTCT
Cd5l-F: CAATTGTGGAGCAGTCATCCAA
Cd5l-R: TTCCGTTCCGTTGCAGTCAA
Loxl4-F: CAGTTGGGTCAAGGGCTAGG
Loxl4-R: AGCCCATGTCTGGGATGTTG
Lrrtm3-F: GCTCCATTCTCTGGGATCGG
Lrrtm3-R: TCCCAGGTCCAGAAGTTCCA
P2rx6-F: CTCGTGACACCAGCTCAAGT
P2rx6-R: GTCCTGTGGGTTCCGTTGAA
Orm3-F: TGGCTGACTCAGACCCTGAT
Orm3-R: GGGTCCCATTCTCTCTCTGG
β-Actin-F: GGCTGTATTCCCCTCCATCG
β-Actin-R: CCAGTTGGTAACAATGCCATGT
Gapdh-F[59]: GAGGGGCCATCCACAGTCTTC
Gapdh-R: CATCACCATCTTCCAGGAGCG

Animals

All animal experimental procedures were conducted in accordance with the Institutional Animal Care and Use Committee of the

Institute of Zoology, Chinese Academy of Sciences (protocol no. IOZ-IACUC-2024-143). *Pd-1*$^{fl/fl}$ mice were generated by the Experimental Animal Center of the Institute of Zoology[60]. *Cd5l*$^{fl/fl}$ mice were generated by Cyagen. *Cx3cr1*-Cre (Jackson Laboratories cat. no. 025524), *Cx3cr1*-CreER (Jackson Laboratories cat. no. 021160), Ai14 (Jackson Laboratories cat. no. 007914), *Cx3cr1*$^{GFP/+}$ (Jackson Laboratories cat. no. 005582), *Tie2*-Cre (obtained from Shanghai Model Organism), *Tmem119*-2A-CreERT2 (Cyagen cat. no. C001327) and Rosa26-iDTR (Cyagen cat. no. C001477) mice were maintained in a C57BL/6 background. *Pd-1*$^{cKO\text{-}cx3}$ mice were generated by crossing *Pd-1*$^{fl/fl}$ mice with *Cx3cr1*-Cre and *Cd5l*$^{cKO\text{-}cx3}$ mice were generated by crossing *Cd5l*$^{fl/fl}$ mice with *Cx3cr1*-Cre. *Pd-1*$^{fl/fl}$ mice were crossed with *Cx3cr1*-CreER and Ai14 mice to obtain *Pd-1*$^{cKO\text{-}cx3ER}$::Ai14. To conditionally knock out the *Pd-1* gene in microglia, *Pd-1*$^{fl/fl}$ mice were crossed with *Tmem119*-2A-CreERT2 and Ai14 mice to obtain *Pd-1*$^{cKO\text{-}TmemER}$::Ai14. To generate *Tie2*-Cre::Ai14::*Cx3cr1*$^{GFP/+}$, *Tie2*-Cre::Ai14 mice were crossed with the *Cx3cr1*$^{GFP/+}$ mice line. Meanwhile, *Tmem119*-CreER::R26-DTR mice were obtained by crossing *Tmem119*-2A-CreERT2 mice with Rosa26-iDTR mice to establish microglia-deficient model mice. Experimental mice were analyzed at postnatal days 5, 7, 11, 13, 14, 20 and 40, comprising an equal number of males and females. Mice were subjected to random allocation, and all data collection and analysis were conducted by researchers blinded to the genotype. All mice were housed with a standard light-controlled (12-h light–dark cycle) at 22–25 °C and provided standard chow ad libitum.

Tamoxifen and PLX5622 injections

For tamoxifen-induced labeling of cells expressing the *Cx3cr1*-genotype, P7 mice were injected intraperitoneally for 3 consecutive days with tamoxifen (0.1 mg g^{-1}, MCE, HY-13757A) dissolved in corn oil. To eliminate microglia, P7 mice were injected intraperitoneally daily for 7 consecutive days with the CSF-1R inhibitor PLX5622 (50 mg kg^{-1}, MedChemExpress, HY-114153).

Diphtheria toxin treatment

P0 mice were injected intraperitoneally for 3 consecutive days with tamoxifen (0.1 mg g^{-1}) to induce the expression of *Tmem119*-2A-CreERT2. Subsequently, to achieve brain microglia depletion during cerebral vascular reconstruction, DT (1 µg, Sigma, D0564) was injected into the brain ventricles of *Tmem119*-CreER::R26-DTR mice for three consecutive days, while PBS was injected into the brain ventricles of *Tmem119*-CreER mice as a control group. At P13, these mice were killed and the cerebral cortex was analyzed.

Isolation and culture of primary mouse microglia

The isolation and culture of primary mouse microglia were performed as previously described[61]. In brief, meninges were removed from P11 newborn brains, then cortices were digested with papain for 30 min at 37 °C. During digestion, the sample was gently shaken every 10 min until they formed a loose organization. After removing papain and washing three times with DMEM, cells were dispersed into a single-cell suspension through a 70-mm pore cell strainer (Corning, 352350). Subsequently, filtered cells were collected and resuspended in ice-cold FACS buffer. Then they were labeled by anti-CD45-PE (BioLegend, 30-F11,103105), anti-CD11b-APC (eBioscience, M1/70, 17-0112-83). According to the manufacturer's instructions, the labeled cells were sorted by FACSCalibur cytometer (Becton Dickinson). Finally, primary mouse microglia were cultured in 12-well or 24-well plates at 37 °C.

Primary neural progenitor cell culture

Cerebral cortices from E13.5 embryos were isolated and digested with papain at 37 °C for 5 min. Papain was then removed and tissues were washed three times with DMEM before the cell suspension was filtered through a 70-µm filter membrane. Following centrifugation at 120*g* for 5 min, cells were resuspended. For proliferation assays, NPCs were seeded into uncoated, low-attachment six-well plates and cultured in proliferation medium until neurospheres appeared. The medium consisted of 50% Neurobasal-A (Invitrogen) and 50% DMEM/F12 (Invitrogen), supplemented with 1% penicillin–streptomycin, 0.5% GlutaMAX, 2% B27 supplement, 1% nonessential amino acids (all from Invitrogen), 10 ng ml^{-1} epidermal growth factor and 10 ng ml^{-1} basic fibroblast growth factor (both from Invitrogen).

Isolation and culture of cortical neurons

Cortical neurons were derived from the cortical plate of E13.5 embryos and plated onto high-attachment six-well plates pre-coated with laminin and poly-D-lysine. Neurons were cultured in neuronal differentiation medium, which comprises low-glucose DMEM (Gibco) supplemented with 1% penicillin–streptomycin, 2% B27 supplement (Invitrogen) and 1% fetal bovine serum (Invitrogen).

Primary mouse brain endothelial cell culture

In brief, E13.5 cerebral cortices were isolated and digested with papain at 37 °C for 5 min. After papain removal, samples were washed three times with DMEM, and the cell suspension was filtered through a sterile 70-µm filter membrane. Filtered cells were collected by centrifugation at 120*g* for 5 min, then resuspended in 1 ml red blood cell lysis buffer (Thermo Fisher Scientific) for 3 min. The cell suspension was overlaid onto DMEM and centrifuged again. Following centrifugation, the cell pellet was resuspended in EC-selective EGM-2 medium (EGM-2 BulletKit; Lonza), and primary ECs were seeded into six-well plates pre-coated with rat tail collagen type I (Thermo Fisher Scientific). Cultures were maintained in EGM-2 medium at 37 °C for 1 week.

Isolation and culture of astrocytes

Astrocytes were isolated and cultured as previously described[62]. E18 cerebral cortices were isolated and digested with papain at 37 °C for 5 min. Following papain removal, samples were washed three times with astrocyte culture medium, and cells were seeded into T75 culture flasks for 14-day incubation at 37 °C. Fresh medium was replaced every 3 days, and microglia were depleted on day 7 via orbital shaking of the flasks at 180 rpm for 30 min. The astrocyte culture medium consisted of high-glucose DMEM (Gibco) supplemented with 10% fetal bovine serum (BIOCHROME) and 1% penicillin–streptomycin (Life Technologies).

Stereotaxic injections

P11 pups were anesthetized by intraperitoneal injection of 2,2,2-tribromoethanol (Sigma, T48402). The body temperature of mice was maintained by using a heating pad during the operation. Surgery was performed with a WPI stereotaxic apparatus and all surgical tools were sterilized before the surgery. For injections into the cerebral cortex, the mice head was fixed in a stereotaxic frame and the incision site was disinfected with 2% iodine and 70% ethanol before surgical procedures. A small craniotomy (~1 mm) was performed on the head of mice with a micro knife. Subsequently, CD5L protein (10 µg ml^{-1}), PD-L1 protein (1 µg, MCE, HY-P70632), PD-L2 protein (1 µg, MCE, HY-P73369), anti-PD-L1 monoclonal antibody (1 µg, BioX Cell, BE0101) or anti-PD-L2 monoclonal antibody (1 µg, BioX Cell, BE0112) were slowly delivered by intracerebroventricular injection into *Pd-1*$^{fl/fl}$ and *Pd-1*$^{cKO\text{-}cx3}$ mice (coordinates, $x = 1$, $y = 1.8$, $z = -1$, from lambda) using a beveled glass needle with ~50-µm outer diameter. And the same volume of water was injected as a control. After 4 h of CD5L protein treatment[28], the mouse brain was taken out for subsequent experiments. Besides, after 1 h of PD-L1/PD-L2 protein treatment[10], the mouse brain was taken out for subsequent experiments.

In vivo live imaging

Cx3cr1$^{GFP/+}$ mice were injected intravenously with Lectin-DyLight 594 to label blood vessels. *Cx3cr1*-CreER::Ai14 and *Pd-1*$^{fl/fl}$::*Cx3cr1*-CreER::Ai14 mice were injected intravenously with Lectin-DyLight 488 (VECTOR, DL-1174-1) to label blood vessels.

Cranial window surgery

P11 pups were anesthetized by intraperitoneal injection of 2,2,2-tribromoethanol and immobilized in a stereotaxic apparatus. Before surgery, the surgical area was disinfected with 2% iodine and 70% alcohol, then the scalp overlying the dorsal skull and periosteum were removed. Subsequently, a circular craniotomy (3 mm in diameter) was drilled with a dental drill. Care was taken not to damage the dura mater and absolutely avoid bleeding during the operation. A 3-mm glass coverslip sterilized with 70% ethanol was placed inside the craniotomy. Finally, the custom-made metal plate was attached to the skull with dental cement. Mice were allowed to recover in their home cages for at least 1 h before starting imaging.

Imaging

In the in vivo imaging experiments, mice were fixed in a customized fixture and then placed on a confocal microscope. We used a ×25/NA water immersion lens (Nikon) to capture images. The optimal wavelength of GFP was 488 nm, and that of tdTomato was 561 nm. Time-lapse images of microglia and cerebral vessels were recorded at 10–200 µm from the cortical surface every 5 min for 2 h and 6 h. The images were collected with a resolution of 512 × 512 pixels.

Phagocytosis assay by slice culturing system

P11 mice were killed and dissected brains were immediately put in pre-cooled microglia culture medium. Sagittal sections with a thickness of 250 µm were prepared by a vibratome, then transferred to a 24-well plate and incubated for 1 h in the incubator (37 °C, 5% CO_2). Then, 0.5 mg ml^{-1} pHrodo Red Zymosan Bioparticles (Thermo Fisher Scientific, P35364) was added to the plate and incubated for 4 h for phagocytosis.

Phagocytosis assay in primary cortical microglia

The fluorescent latex microbeads (Sigma-Aldrich, L2778) were added to isolated primary microglia and incubated for 4 h in the incubator (37 °C, 5% CO_2) for phagocytosis. After washing with PBS and fixing with 4% PFA for 20 min at room temperature, F-actin was stained with phalloidin and cells were observed under a fluorescence microscope.

Three-dimensional reconstruction

The 40-µm brain sections labeled with anti-Iba1 and anti-CD68 were used to obtain confocal images on Zeiss LSM880 microscope with ×63 oil objective. Microglia were scanned from top to bottom with a step size of 0.85 µm in the *z* direction. The $Iba1^+$ microglia were randomly tracked from the confocal images using Imaris v.9.7 software, and the microglia were reconstructed in 3D using the 'surface' function in Imaris.

Engulfment analysis

Processing of ×63 images stained for Iba1 and CD68 was performed in Imaris v.9.7 software. For each genotype, $n \geq 3$ animals were imaged. Using the 'surface' function in Imaris v.9.7, $Iba1^+$ cells and $CD68^+$ lysosomes were reconstructed in 3D and their volumes were measured. Any CD68 signal outside the $Iba1^+$ cells was masked in the image using the mask function. Lysosome content was defined as the percentage of $CD68^+$ lysosome volume relative to $Iba1^+$ cell volume.

Quantitative analysis of microglia–brain vessel contact

Processing of ×63 images stained for Iba1 and IB4/CD31 was performed in Imaris v.9.7. Next, the image was cropped into an image containing single microglia enwrapping the cerebral vessels. The 'Coloc' label was used to create a new colocalization channel (a channel describing the overlap of $Iba1^+$ and $IB4^+$/*Tie2*-Cre::tdTomato signals in Imaris v.9.7e). We measured the volume of the overlapping area using the 'Surface' function in Imaris v.9.7; the volume of $Iba1^+$ cells was also measured using the 'Surface' function. Finally, the proportion of the overlapping volume between $Iba1^+$ cells and $IB4^+$/$CD31^+$ cells to total $Iba1^+$ cells was evaluated.

Mouse brain slice preparation

Mice were anesthetized and then decapitated to take out their brains. Then, 300-µm brain slices were prepared with a vibratome (Campden Instruments, 7,000 smz) and transferred to a 12-well plate containing culture medium. To assess the release of PD-L1 and PD-L2 proteins, we placed three 300-µm mouse brain sections together and cultured them in a 37 °C cell culture incubator for 1 h. The supernatant was collected for PD-L1 and PD-L2 ELISA.

ELISA

Primary microglia in the cerebral cortex of P11 mice were isolated and cultured for 2 days, and then cell samples were collected and detected according to the mouse CD5 antigen-like (CD5L) ELISA kit (Abebio, AE51323MO). PD-L1 and PD-L2 ELISA experiments were performed using the mouse PD-L1 ELISA kit (Solarbio, SEKM-0259) and the mouse PD-L2 ELISA kit (ZOKEYO Y-99472).

Oxygen saturation level detection experiment

Mice anesthetized with 2.5% isoflurane were placed on a heated imaging platform under the photoacoustic imaging (PAI) transducer, and ultrasound (US) gel was applied to the top of the brain to facilitate US imaging transmission. High-resolution US and PAI were obtained by an ultrasound-photoacoustic high-resolution multimodal imaging system (Vevo F2 LAZR-X). PAI was performed using the following parameters: wavelength range, 750/850 nm; frequency, 15–29 MHz; depth, 20 mm; width, 14 mm; and acquisition mode, sO_2/Hbt. The sO_2 level was estimated by obtaining 3D PA images of the mouse brain. Simultaneously, the B model was used to perform ultrasound image acquisition. All imaging data were processed using the Visualsonics workstation suite (VevoLab).

The blood flow measurement experiment

The scalp of mice anesthetized with 2.5% isoflurane was removed to expose their skulls. The blood perfusion was recorded by RFLSI-ZW laser speckle contrast imaging system (RWD).

RNA sequencing

Total RNA of P11 primary mouse brain microglia of *Pd-1*$^{fl/fl}$ and *Pd-1*$^{cKO\text{-}cx3}$ mice was extracted by the TRIzol method (Invitrogen). RNA was quantified by Agilent 2100 Bioanalyzer (Annoroad Genomics), and then high-throughput sequencing was performed by Illumina HiSeq 2500 platform (Annoroad Genomics).

Statistical analysis

Most experiments were performed using three or more independent biological replicates. Statistical analyses were conducted using GraphPad Prism v.6.0 software. For comparisons between two groups, statistical significance was calculated using an unpaired two-tailed Student's *t*-test. For analyses involving two groups, one-way ANOVA was applied, followed by Dunnett's test (comparing all groups to a control) or Tukey's Test (comparing all pairs of groups). For longitudinal or matched data, repeated-measures two-way ANOVA was employed, followed by Bonferroni's multiple comparisons test. For specific categorical data assessments, a two-tailed modified Fisher's exact test was used, with multiple hypothesis testing corrections applied via the Benjamini–Hochberg false discovery rate method. Data distribution was assumed to be normal but this was not formally tested. All data were collected randomly, and mice were randomly allocated during the experiment. No statistical methods were used to predetermine sample sizes but our sample sizes are similar to those reported in previous publications[5,24]. No animals or data were excluded from the analysis.

Reporting summary
Further information on research design is available in the Nature Portfolio Reporting Summary linked to this article.

Data availability
The raw data reported in this paper are accessible in NCBI's Sequence Read Archive under accession code SRP530538. Source data are provided with this paper.

Code availability
No custom software codes were used to analyze the data.

References

59. Kim, H. I. et al. *Gardenia jasminoides* ameliorates antibiotic-associated aggravation of DNCB-induced atopic dermatitis by restoring the intestinal microbiome profile. *Nutrients* https://doi.org/10.3390/nu13041349 (2021).
60. Ji, F. et al. Brain-specific PD1 deficiency leads to cortical neurogenesis defects and depressive-like behaviors in mice. *Cell Death Differ.* **30**, 2053–2065 (2023).
61. Li, Z. & Zhang, C. J. Isolation and culture of mouse primary microglia and oligodendrocyte precursor cells. *Methods Mol. Biol.* **2782**, 167–173 (2024).
62. Schildge, S., Bohrer, C., Beck, K. & Schachtrup, C. Isolation and culture of mouse cortical astrocytes. *J. Vis. Exp.* https://doi.org/10.3791/50079 (2013).

Acknowledgements
We thank W.-Z. Sun (Chinese Institute for Brain Research, Beijing) for technical support with the craniotomy surgery for in vivo imaging. We also thank the members of the Jiao laboratory for insightful discussions and valuable comments.

Author contributions
M.Z., Y.W. and J.J. completed the experiments together. M.Z. completed the phenotype determination of previous experiments. Y.W. provided the research of the later mechanism and the rescue experiment, which was completed under the guidance of J.J. and F.J. In addition, R.Y. performed experiments on microglia and cerebrovascular function in weaning and adult mice. S.L. and C.L. provided assistance in plasmid construction. X.Z. and R.Y. performed the identification of mice. H.L. provided guidance on experiments monitoring blood flow and blood oxygen levels in mice. M.Z. wrote the manuscript with input from all authors. J.J. supervised the project and obtained funding support.

Funding
This work was supported by the National Key R&D Program of China (2024YFA1802600 to J.J., 2025YFA1805100 to F.J., 2024YFA1802202 to J.J., 2021YFA1101402 to F.J., 2023YFA1801500 to Z.L., and 2024YFA1107500 to Y.L.), the National Natural Science Foundation of China (32521008, 32230040, 32450088, 92368203, and 92468302 to J.J.; 32501026 to Y.W.; 32300949 to Z.L.; 32300671 to Y.L.; and 32200648 to L.S.), the Changping Laboratory (to J.J.), the China Postdoctoral Science Foundation (2024T170917 to Z.L.), the Initiative Scientific Research Program of Institute of Zoology, Chinese Academy of Sciences (2023IOZ0304 to F.J. and 2024IOZ0104 to J.J.), and the Key Laboratory of Organ Regeneration and Reconstruction, Chinese Academy of Sciences (2024KF04 to J.J.). The funders had no role in study design, data collection and analysis, decision to publish or preparation of the manuscript.

Competing interests
The authors declare no competing interests.

Additional information
Extended data is available for this paper at https://doi.org/10.1038/s41593-026-02378-x.

Supplementary information The online version contains supplementary material available at https://doi.org/10.1038/s41593-026-02378-x.

Correspondence and requests for materials should be addressed to Jianwei Jiao.

Peer review information *Nature Neuroscience* thanks Ukpong Eyo and the other, anonymous, reviewer(s) for their contribution to the peer review of this work.

https://doi.org/10.1038/s41593-026-02378-x

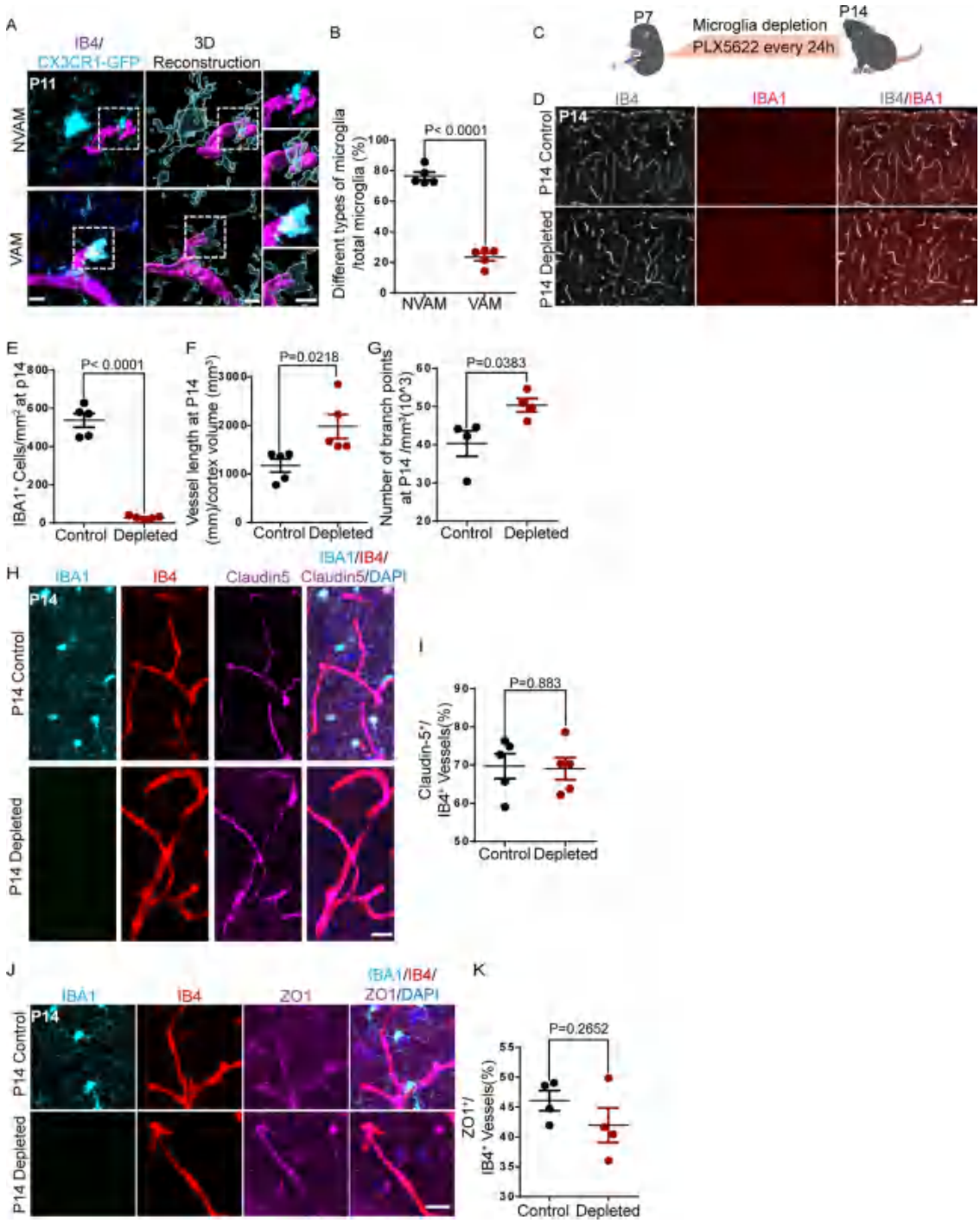

Extended Data Fig. 1 | The impact of microglia depletion on cerebral vascular development. (**A**) Confocal images and reconstructions of microglia-cerebrovascular interactions include "NVAM" and "VAM" at P11. Non-vessel-associated microglia (NVAM): the proportion of the overlapping volume between microglia and cerebral blood vessels to the total volume of microglia was less than 30%; Vessel-associated microglia (VAM): the proportion of the overlapping volume between microglia and cerebral blood vessels to the total volume of microglia was more than 30%. The right insets indicated higher magnification images of the delineated areas. Scale bars, 5 μm. (**B**) Statistics on the proportion of different types of microglia in the total microglia. $n = 5$ brain slices from 5 mice. (**C**) Schematic of microglia depletion during P7 to P14. (**D**) Immunofluorescence staining for IB4 and IBA1 in control and depleted mice at P14. Scale bars, 50 μm. (**E**) The graph showed significantly decreased IBA1$^+$ cells in depleted mice. $n = 5$ brain slices from 5 mice. Quantification of the vessels length (**F**) and the number of branch points (**G**) in control and depleted mice at P14. $n = 5$ brain slices from 5 mice in vessels length and $n = 4$ brain slices from 4 mice in the number of branch points. (**H**) Confocal images of claudin-5 for tight junction in cerebral vessels at P14. Scale bars, 20 μm. (**I**) Quantification analysis of the proportion of Claudin-5 showed no changes in control and depleted mice. $n = 5$ brain slices from 5 mice. (**J**) Confocal images of ZO1 for tight junction in cerebral vessels at P14. Scale bars, 20 μm. (**K**) Quantification analysis of the proportion of ZO1 showed no changes in control and depleted mice. $n = 4$ brain slices from 4 mice. For (**B**), (**E**)-(**G**), (**I**) and (**K**) were analyzed using two-tailed unpaired t-test. Data are presented as mean ± s.e.m. for all statistical analyses.

https://doi.org/10.1038/s41593-026-02378-x

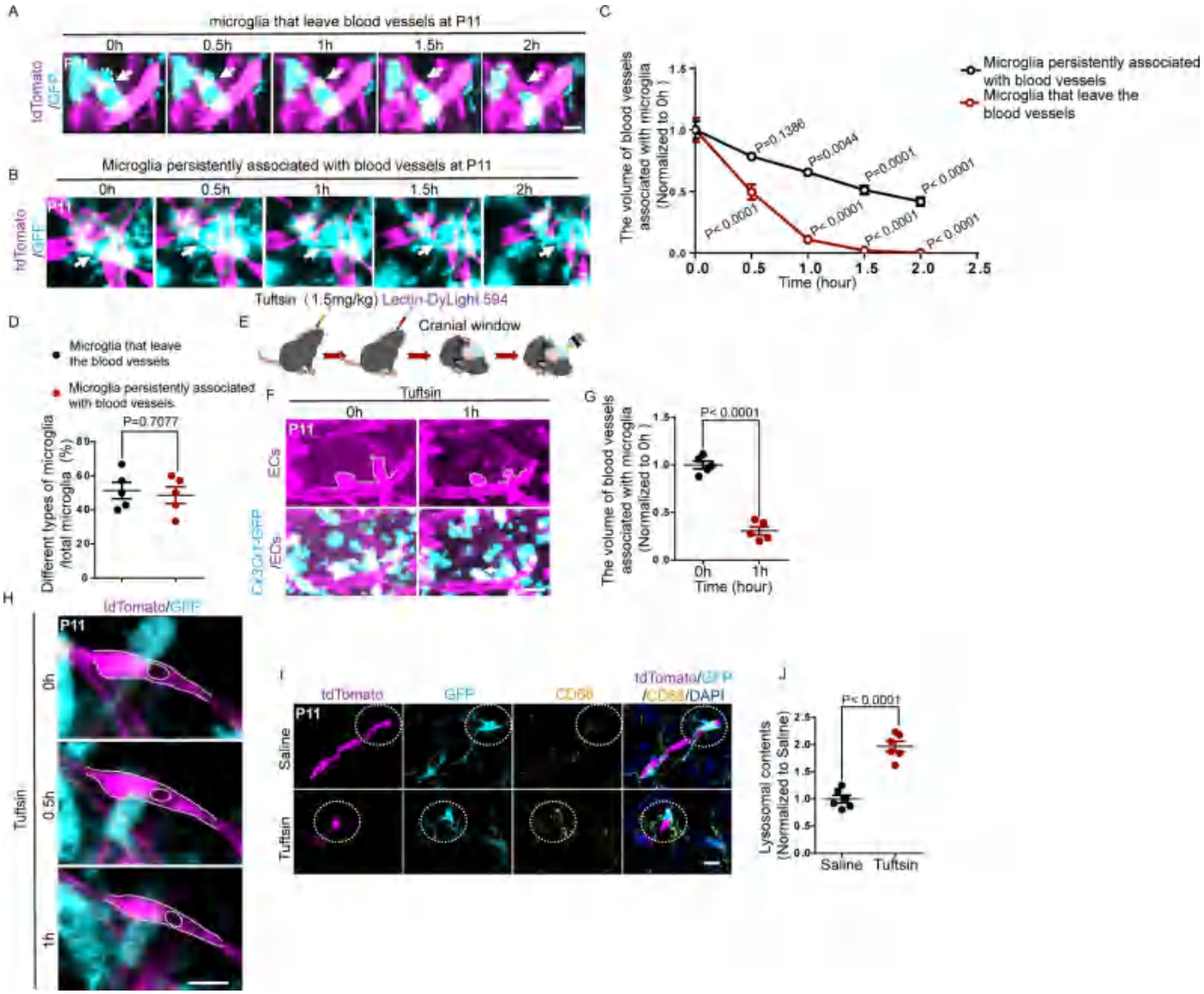

Extended Data Fig. 2 | Microglia phagocytose cerebral vessels during development. (**A**)Time-lapse imaging of microglia that left the brain vasculature within 2 hours at P11. Scale bars, 10 μm. (**B**) Time-lapse imaging showed that microglia persistently associated with blood vessels within 2 hours at P11. Scale bars, 3um. (**C**) The change of cerebral vascular volume associated with or not associated with microglia. *n* = 5 mice per group. (**D**) The statistical graph showed that the proportion of microglia leaving the cerebral blood vessels or continuing to associate with the cerebral blood vessels was similar. n = 5 cells from 5 mice. (**E**) In order to activate microglia, Tuftsin was injected into the temporal (or facial) vein of *Cx3Cr1*$^{GFP/+}$ mice, and then lectin 594 was injected intravenously and craniotomy was performed to prepare the cranial window for in vivo imaging. (**F**) Time-lapse images of cerebral vessels associated with microglia after intravenous injection of Tuftsin in *Cx3Cr1*$^{GFP/+}$ mice at P11. Scale bars, 20 μm. (**G**) Statistics showed that the phagocytosis process of microglia on blood vessels was accelerated after Tuftsin treatment. n = 5 mice per group. (**H**) The volume changes in cerebral vessels not associated with microglia after intravenous injection of Tuftsin in *Tie2*-Cre::Ai14::*Cx3Cr1*$^{GFP/+}$ mice at P11. Scale bars, 20 μm. (**I**) Confocal images of microglia (GFP, blue) containing lysosomes (CD68, yellow) after intravenous injection of Tuftsin at P11. Scale bars, 10 μm. (**J**) Quantification analysis of lysosomal contents. n = 6 cells from 6 mice. For (**C**) was analyzed using Repeated-Measures Two-Way ANOVA with Bonferroni's Test. For (**D**), (**G**) and (**J**) were analyzed using two-tailed unpaired t-test. Data are presented as mean ± s.e.m. for all statistical analyses.

https://doi.org/10.1038/s41593-026-02378-x

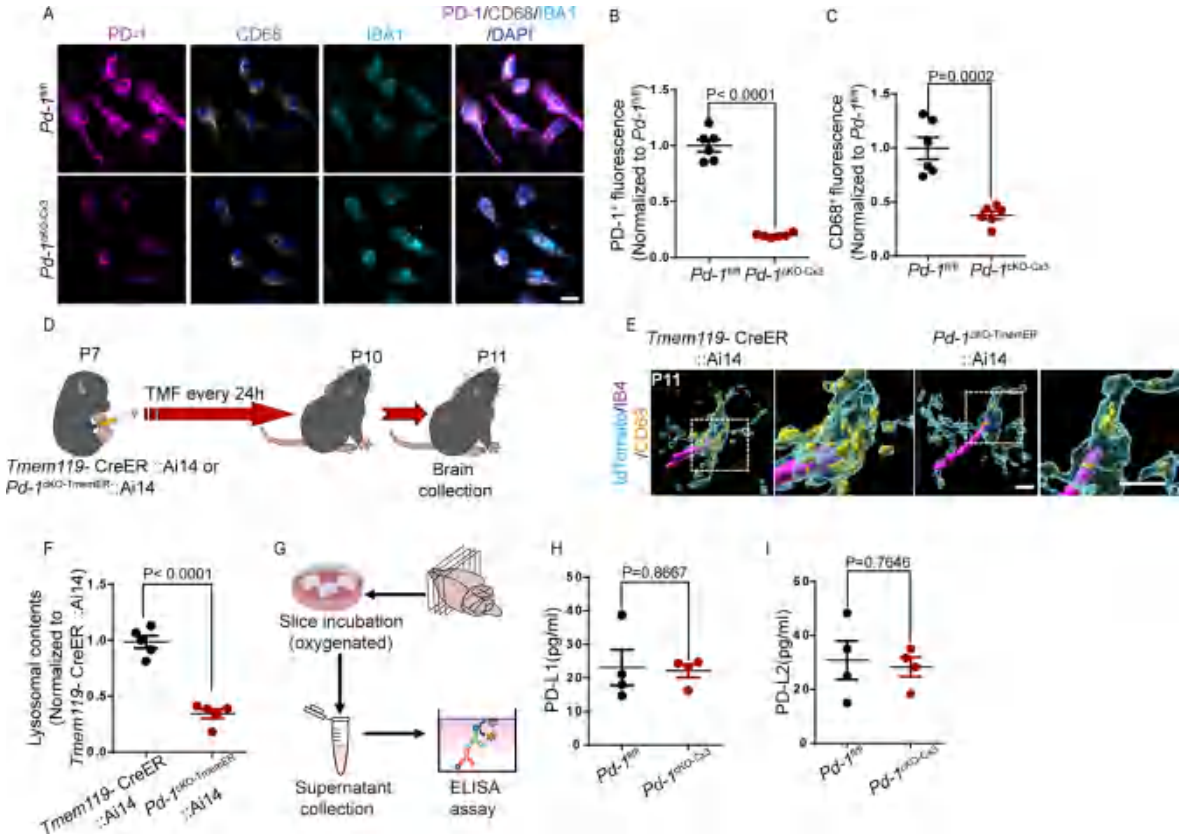

Extended Data Fig. 3 | PD-1 deficiency impairs the phagocytic capacity of microglia. (**A**) PD-1 was co-labeled with CD68 and IBA1 in the *Pd-1*$^{fl/fl}$ and *Pd-1*$^{cKO-Cx3}$ microglia. Scale bars, 10 μm. Quantification analysis of PD-1^{+} fluorescence (**B**) and CD68^{+} fluorescence (**C**) in the *Pd-1*$^{fl/fl}$ and *Pd-1*$^{cKO-Cx3}$ microglia. n = 6 cells from 6 mice. (**D**) *Tmem119*-CreER::Ai14 and *Pd-1*$^{cKO-TmemER}$::Ai14 mice were injected with TMF intraperitoneally every day from P7 to P10, and brain tissue was collected on P11. (**E**) Immunofluorescence staining showed the CD68^{+} lysosomes content in *Tmem119*-CreER::Ai14 and *Pd-1*$^{cKO-TmemER}$::Ai14 microglia at P11. Scale bars, 2um. (**F**) The statistical graph revealed that lysosomes content in *Pd-1*$^{cKO-TmemER}$::Ai14 microglia was decreased significantly. n = 5 cells from 5 mice. (**G**) Schematic of PD-L1 and PD-L2 released from brain slices. (**H-I**) ELISA showed that PD-L1 and PD-L2 ligands were not affected after PD-1 deletion in microglia. n = 4 mice per group. For (**B**)-(**C**), (**F**) and (**H**)-(**I**) were analyzed using two-tailed unpaired t-test. Data are presented as mean ± s.e.m. for all statistical analyses.

https://doi.org/10.1038/s41593-026-02378-x

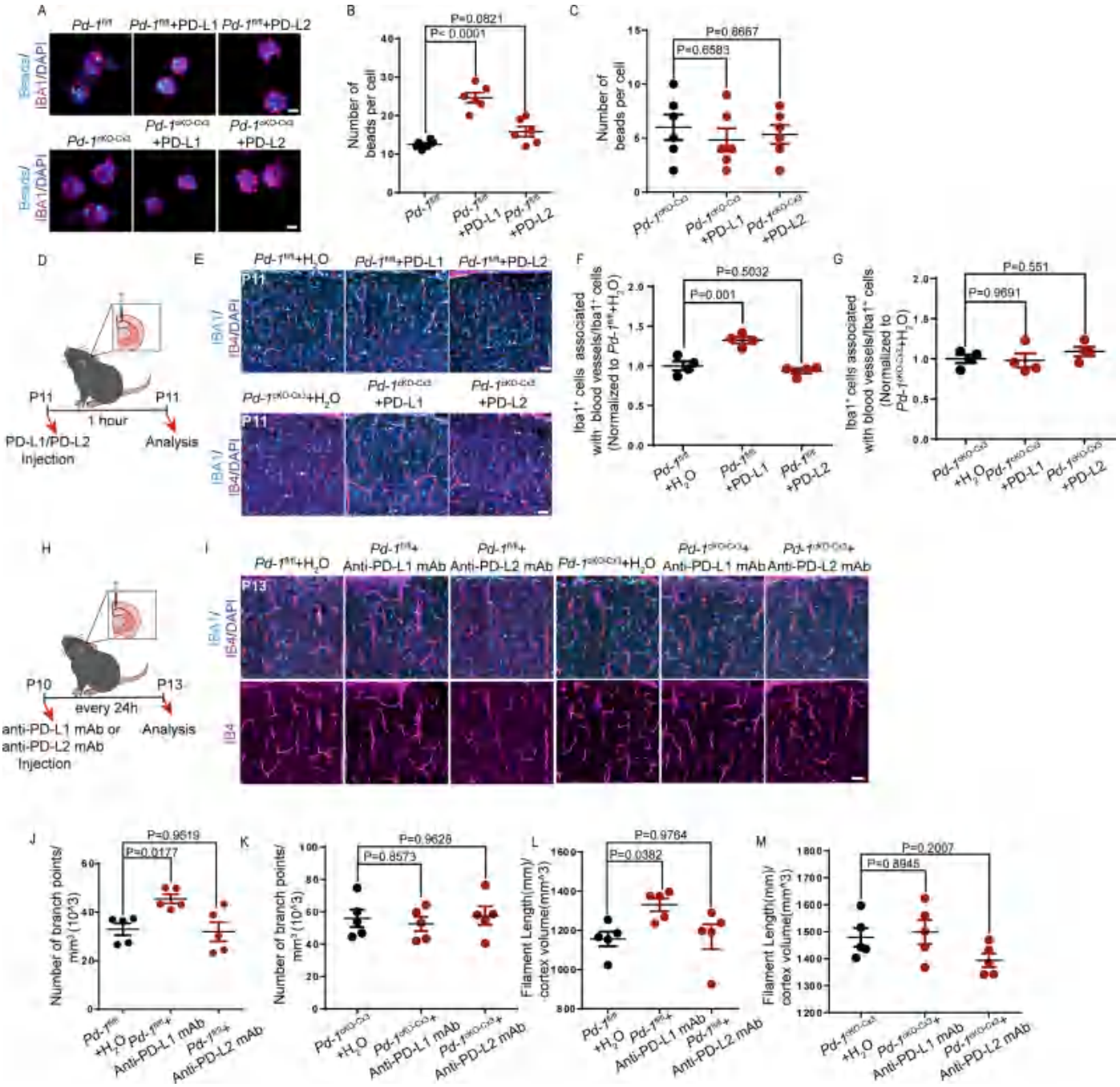

Extended Data Fig. 4 | PD-L1/PD-1 checkpoint pathway regulates the microglia phagocytosis. (**A**) The detection of primary microglia phagocytic capacity after exogenous PD-L1/PD-L2 proteins addition. Scale bars, 5 μm. (**B**-**C**) Quantitative analysis of *Pd-1*$^{fl/fl}$ and *Pd-1*$^{cKO\text{-}Cx3}$ microglia phagocytosis after exogenous addition of PD-L1/PD-L2 protein. n = 6 cells from 6 mice. (**D**) Scheme illustrated PD-L1/PD-L2 protein was injected into *Pd-1*$^{fl/fl}$ or *Pd-1*$^{cKO\text{-}Cx3}$ mice at P11, tissues were collected and analyzed after 1 hours. Mice brain ventricles were injected with equal volume of water as control group. (**E**) Confocal immunofluorescence image of cerebral vessels (IB4, purple) and microglia (IBA1, blue) after injection of PD-L1/PD-L2 protein. Scale bars, 50 μm. (**F**-**G**) Quantitative analysis of vessel-associated IBA1$^+$ cells in all IBA1$^+$ cells after injection of PD-L1/PD-L2 protein. n = 4 brain slices from 4 mice. (**H**) Scheme illustrated anti-PD-L1 mAb or anti-PD-L2 mAb was injected daily into *Pd-1*$^{fl/fl}$ and *Pd-1*$^{cKO\text{-}Cx3}$ mice from P10 to P13. Mice brain ventricles were injected with equal volume of water as control group. (**I**) Confocal immunofluorescence image of cerebral vessels (IB4, purple) and microglia (IBA1, blue) after injection of anti-PD-L1 mAb or anti-PD-L2 mAb. Scale bars, 50 μm. Quantification of the branch points (**J**-**K**) and vessel length (**L**-**M**) after injection of anti-PD-L1 mAb or anti-PD-L2 mAb. n = 5 brain slices from 5 mice. For (**B**)-(**C**), (**F**)-(**G**) and (**J**)-(**M**) were analyzed using One-Way ANOVA with Dunnett's Test. Data are presented as mean ± s.e.m. for all statistical analyses.

https://doi.org/10.1038/s41593-026-02378-x

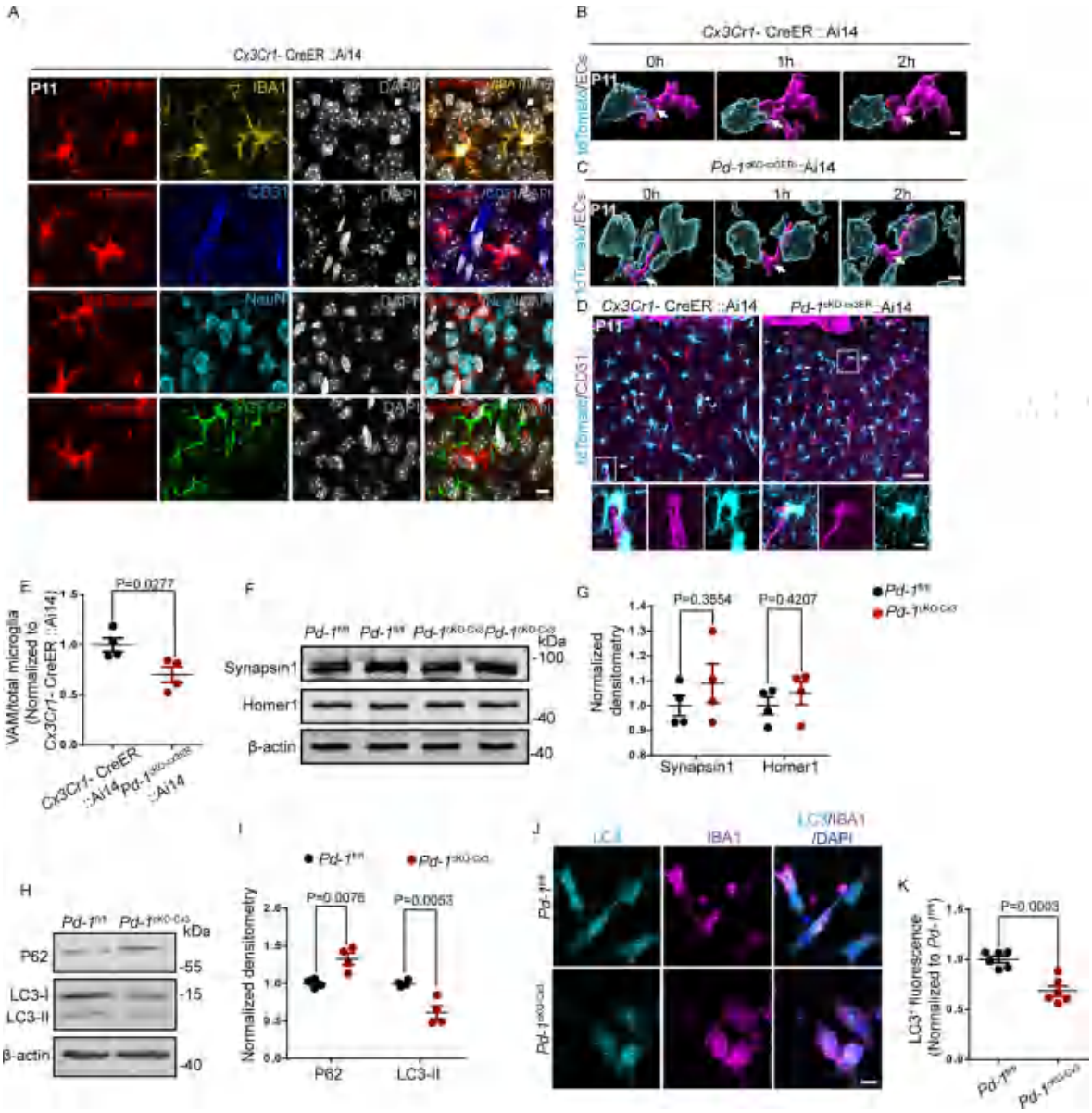

Extended Data Fig. 5 | *Cx3Cr1*-CreER::Ai14 specifically label microglia and autophagy of lysosomes is affected by the loss of PD-1 in microglia. (**A**) Confocal images showed that *Cx3Cr1*-CreER::Ai14 mice were induced by tamoxifen and only specifically labeled microglia (IBA1, yellow), but not blood vessels (CD31, blue), neurons (NeuN, azury) and astrocytes (GFAP, green). Scale bars, 10 μm. These results were independently repeated in 3 separate experiments from 3 mice, and consistent findings were obtained. (**B**) Time-lapse imaging of microglia that left the brain vasculature within 2 hours in *Cx3Cr1*-CreER::Ai14 mice at P11. Scale bars, 5 μm. These results were independently repeated in 3 separate experiments from 3 mice, and consistent findings were obtained. (**C**) Time-lapse imaging of microglia that continuous to associate with the brain vasculature within 2 hours in *Pd-1*$^{cKO\text{-}Cx3ER}$::Ai14 mice at P11. Scale bars, 5 μm. These results were independently repeated in 3 separate experiments from 3 mice, and consistent findings were obtained. (**D**) Confocal immunofluorescence image of cerebral vessels (CD31, purple) and microglia (tdTomato, blue). Scale bars, 50 μm (overview) and 10 μm (inset and rendering). (**E**) Quantitative analysis of VAM in all microglia at P11. n = 4 brain slices from 4 mice. (**F**) Synapse-specific markers Synapsin1 and Homer1 protein levels. (**G**) Quantification of Synapsin1 and Homer1 protein levels. n = 4 mice per group. (**H**) Western blotting analysis the expression levels of P62 and LC3 in microglia. (**I**) Quantification of P62 and LC3-II normalized densitometry. n = 4 mice per group. (**J**) High-magnification confocal images of LC3^{+} IBA1^{+} cells in microglia. Scale bars, 10 μm. (**K**) Quantification of LC3^{+} fluorescence in microglia. n = 6 cells from 6 mice. For (**E**), (**G**), (**I**), and (**K**) were analyzed using two-tailed unpaired t-test. Data are presented as mean ± s.e.m. for all statistical analyses.

https://doi.org/10.1038/s41593-026-02378-x

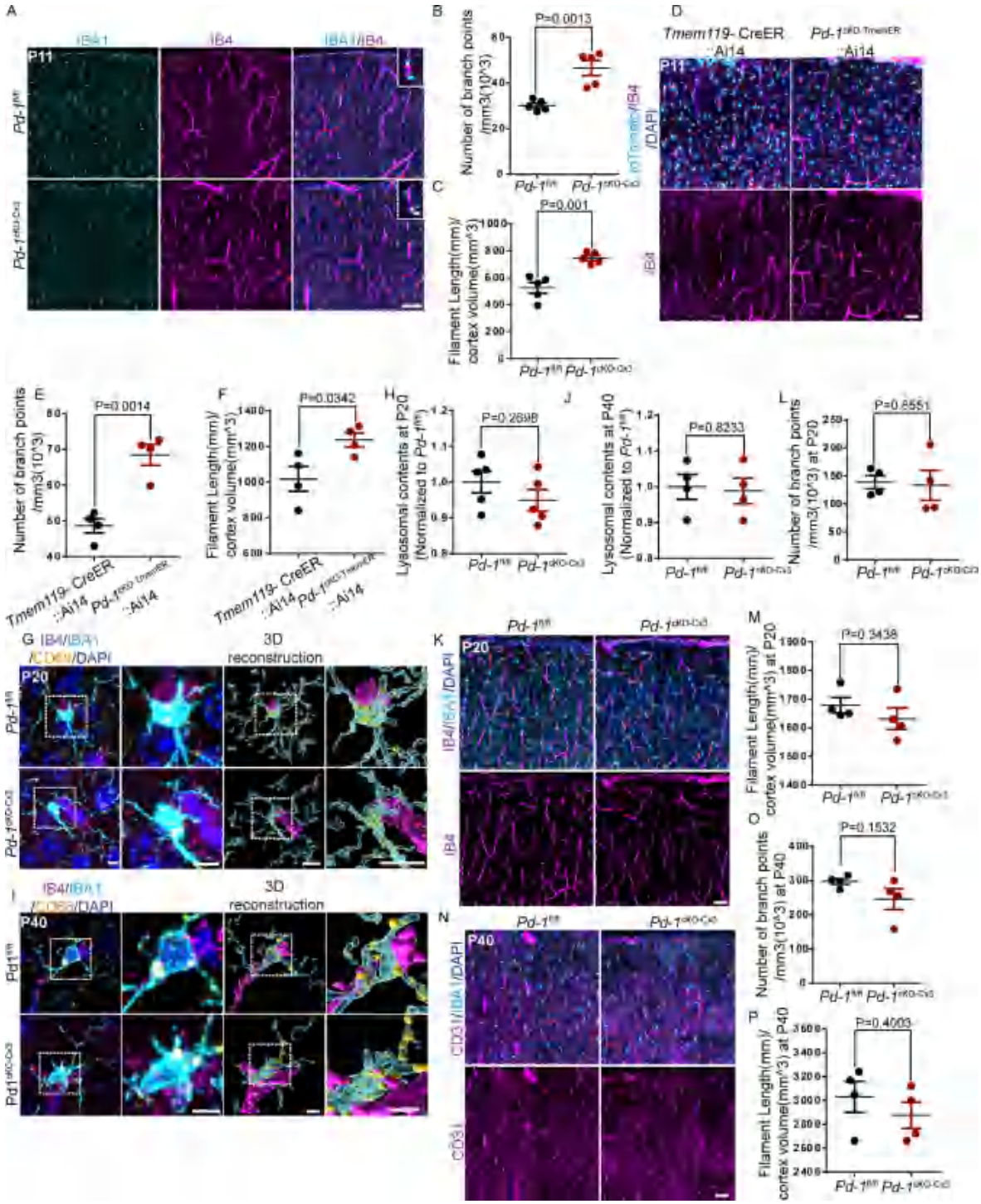

Extended Data Fig. 6 | The effects of *Pd-1* deficiency in microglia on cerebral blood vessels disappear during weaning. (**A**) Representative images of microglia (IBA1, blue) and cerebral vessels (IB4, purple) at P11. Scale bars, 100 μm (overview) and 10 μm (inset and rendering). Quantification of the number of branch points (**B**) and the filament length (**C**) in *Pd-1*$^{fl/fl}$ and *Pd-1*$^{cKO\text{-}Cx3}$ brain cortex at P11. n = 5 brain slices from 5 mice. (**D**) Confocal images of microglia (tdTomato, blue) and cerebral vessels (IB4, purple) in *Tmem119*-CreER::Ai14 and *Pd-1*$^{cKO\text{-}TmemER}$::Ai14 brain cortex at P11. Scale bars, 50 μm. Quantification of the number of branch points (**E**) and the filament length (**F**) in *Tmem119*-CreER::Ai14 and *Pd-1*$^{cKO\text{-}TmemER}$::Ai14 brain cortex at P11. n = 4 brain slices from 4 mice. (**G**) Images and reconstruction of microglia containing lysosomes at P20. The images on the right were enlarged versions. Scale bars, 10 μm. (**H**) Quantification the lysosomal contents in vessel-associated IBA1$^+$ cells at P20. n = 5 cells from 5 mice. (**I**) Images and reconstruction of microglia containing lysosomes at P40. The images on the right were enlarged versions. Scale bars, 5 μm. (**J**) Quantification the lysosomal contents in vessel-associated IBA1$^+$ cells at P40. n = 4 cells from 4 mice. (**K**) The branch points and filament length of cerebral blood vessels were unchanged after *Pd-1* deficiency in IBA1$^+$ cells at P20. Scale bars, 50 μm. Quantification of the number of branch points (**L**) and the filament length (**M**) at P20. n = 4 brain slices from 4 mice. (**N**) Confocal immunofluorescence image of cerebral vessels (CD31, purple) and microglia (IBA1, blue) at P40. Scale bars, 50 μm. Quantification of the number of branch points (**O**) and the filament length (**P**) at P40. n = 4 brain slices from 4 mice. For (**B**), (**C**), (**E**)-(F), (**H**), (**J**), (**L**), (**M**) and (**O**)-(**P**) were analyzed using two-tailed unpaired t-test. Data are presented as mean ± s.e.m. for all statistical analyses.

https://doi.org/10.1038/s41593-026-02378-x

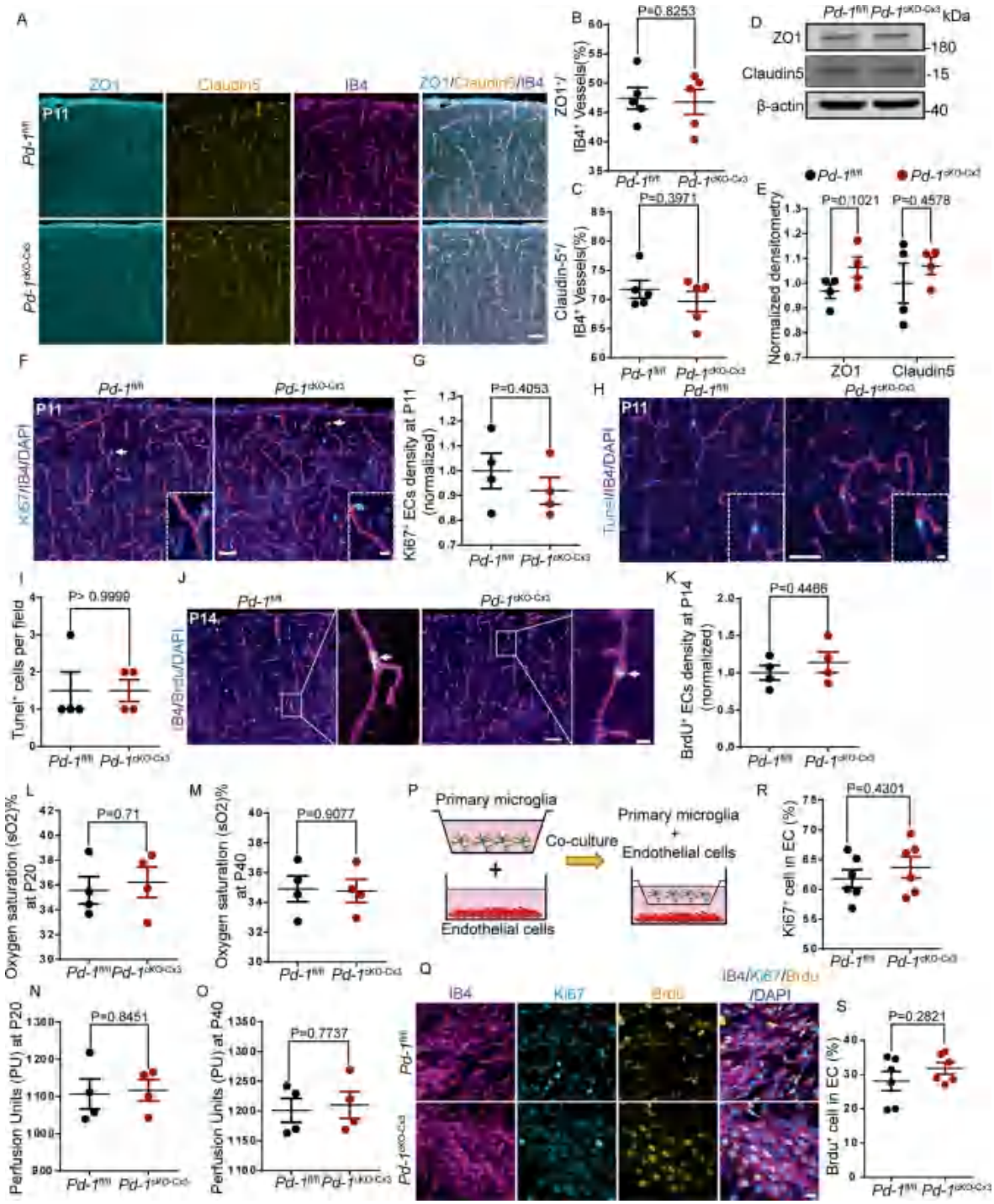

Extended Data Fig. 7 | The changes of cerebral vascular structure after PD-1 deletion in microglia. (**A**) Confocal images showed that the tight junction of cerebral vessels was normal at P11. Scale bars, 50 μm. (**B**) Statistics on the proportion of ZO1$^+$ cerebral vessels in total vessels at P11. n = 5 brain slices from 5 mice. (**C**) Quantitative analyses of the proportion of Claudin-5$^+$ cerebral vessels in total vessels at P11. n = 5 brain slices from 5 mice. (**D**) Western blot analysis of the ZO1 and Claudin-5 protein levels. (**E**) Quantification of the ZO1 and Claudin-5 protein levels. n = 4 mice per group. (**F**) Representative images showed that Ki67 remained unchanged at P11. Scale bars, 50 μm (overview) and 10 μm (inset and rendering). (**G**) Quantification of Ki67$^+$ ECs density. n = 4 brain slices from 4 mice. (**H**) Confocal immunofluorescence images of Tunel$^+$ ECs. Scale bars, 50 μm (overview) and 10 μm (inset and rendering). (**I**) Density of Tunel$^+$ DAPI $^+$ cells per field in blood vessels. n = 4 brain slices from 4 mice. (**J**) Confocal immunofluorescence images of BrdU$^+$ ECs at P14. Scale bars, 50 μm (overview) and 10 μm (inset and rendering). (**K**) Quantification of the BrdU$^+$ ECs density at P14. n = 4 brain slices from 4 mice. (**L**-**M**) The oxygen saturation in cerebral vessels was similar at P20 and P40. n = 4 mice per group. (**N**-**O**) The blood perfusion in cerebral vessels was similar at P20 and P40. n = 4 mice per group. (**P**) Schematic the co-culture system of primary microglia and endothelial cells. (**Q**) Confocal images of ECs (IB4, purple) stained for Ki67 (blue) and Brdu (yellow) in indirect co-culture system. Scale bars, 20 μm. (**R**) Quantitative analysis showed that there was no difference in Ki67$^+$ ECs. n = 6 mice per group. (**S**) The bar graph showed that Brdu$^+$ ECs were similar. n = 6 mice per group. For (**B**), (**C**), (**E**), (**G**), (**I**), (**K**), (**L**)-(**O**) and (**R**)-(**S**) were analyzed using two-tailed unpaired t-test. Data are presented as mean ± s.e.m. for all statistical analyses.

https://doi.org/10.1038/s41593-026-02378-x

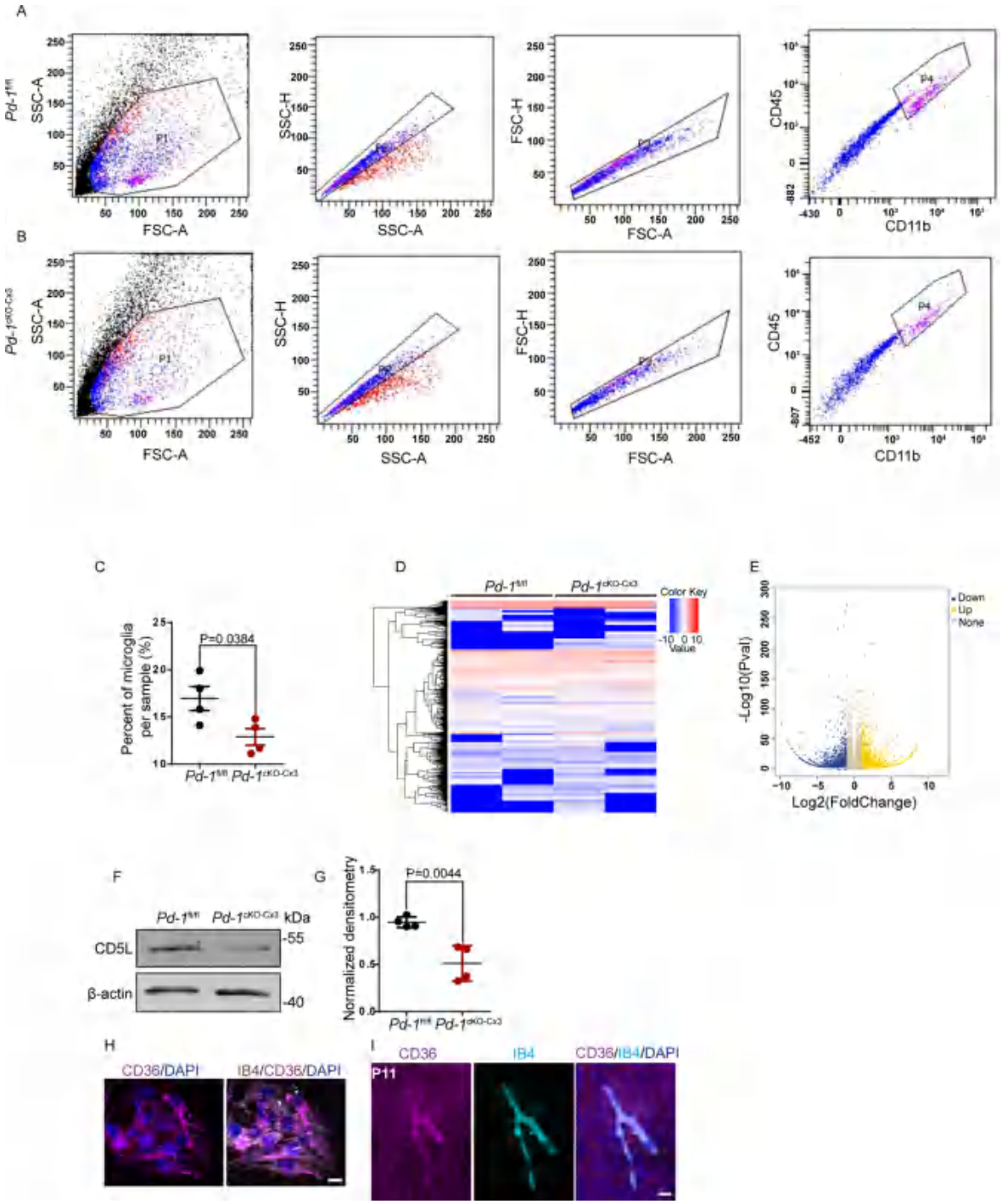

Extended Data Fig. 8 | Loss of PD-1 leads to decreased expressions of CD5L in microglia. (**A-B**) The representative flow cytometry diagram of microglia from *Pd-1*$^{fl/fl}$ and *Pd-1*$^{cKO\text{-}Cx3}$ mice by flow sorting. (**C**) Quantification of the percent of microglia in the *Pd-1*$^{fl/fl}$ and *Pd-1*$^{cKO\text{-}Cx3}$ brain cortex. n = 4 mice per group. (**D**) Heatmap illustrated global genes were sorted by fold change. (**E**) Volcano plots showed the downregulated (blue) and upregulated (yellow) genes in the *Pd-1*$^{fl/fl}$ and *Pd-1*$^{cKO\text{-}Cx3}$ microglia. (**F**) The protein level of CD5L decreased substantially after PD-1 was conditionally knocked out by microglia. (**G**) The bar graph showed CD5L normalized densitometry. n = 4 mice per group. (**H**) CD36 was co-labeled with IB4 in cultured cells. Scale bars, 10 μm. These results were independently repeated in 3 separate experiments from 3 mice, and consistent findings were obtained. (**I**) CD36 was co-labeled with IB4 in mouse cerebral cortex at P11. Scale bars, 10 μm. These results were independently repeated in 3 separate experiments from 3 mice, and consistent findings were obtained. For (**C**) and (**G**) were analyzed using two-tailed unpaired t-test. Data are presented as mean ± s.e.m. for all statistical analyses.

https://doi.org/10.1038/s41593-026-02378-x

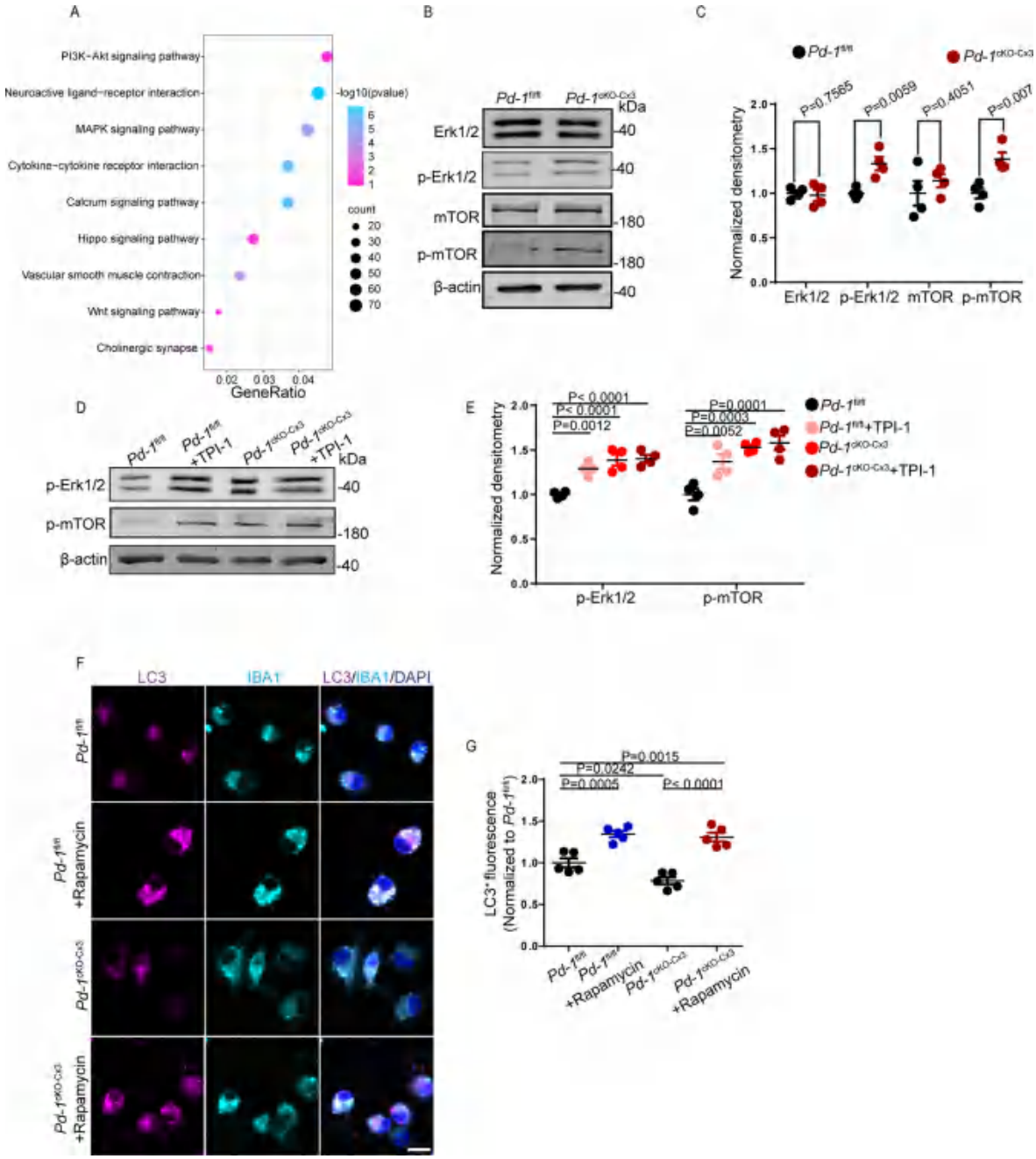

Extended Data Fig. 9 | Microglia assist in sculpting cerebral vessels through the Erk1/2–mTOR signaling pathway. (**A**) Kyoto Encyclopedia of Genes and Genomes (KEGG) pathway analysis on the RNA-seq dataset showed that the MAPK signaling pathway was dramatically enriched. The protein levels of MAPK (Erk1/2), p-MAPK (p-Erk1/2), mTOR and p-mTOR in isolated microglia from *Pd-1*$^{fl/fl}$ and *Pd-1*$^{cKO\text{-}Cx3}$ mice were detected (**B**) and quantified (**C**) by western blotting. n = 4 mice per group. (**D**) Western blot analysis showed that TPI-1(100 ng ml^{-1}, MCE, HY-100463), an inhibitor of SHP-1, could increase the levels of p-Erk1/2 and p-mTOR protein in microglia. (**E**) Quantitative analysis of p-Erk1/2 and p-mTOR protein levels. n = 4 mice per group. (**F**) Representative confocal images of microglia labeled with LC3 and IBA1 after 24 hours of rapamycin (100 nM, MCE, HY-10219) treatment. Scale bars, 10 μm. (**G**) Quantitative analysis of LC3 fluorescence in microglia treated with Rapamycin for 24 hours. n = 5 cells from 5 mice. For (**C**) was analyzed using two-tailed unpaired t-test. For (**E**) was analyzed using One-Way ANOVA with Dunnett's Test. For (**G**) was analyzed using One-way ANOVA with Tukey's Test. Data are presented as mean ± s.e.m. for all statistical analyses.

https://doi.org/10.1038/s41593-026-02378-x

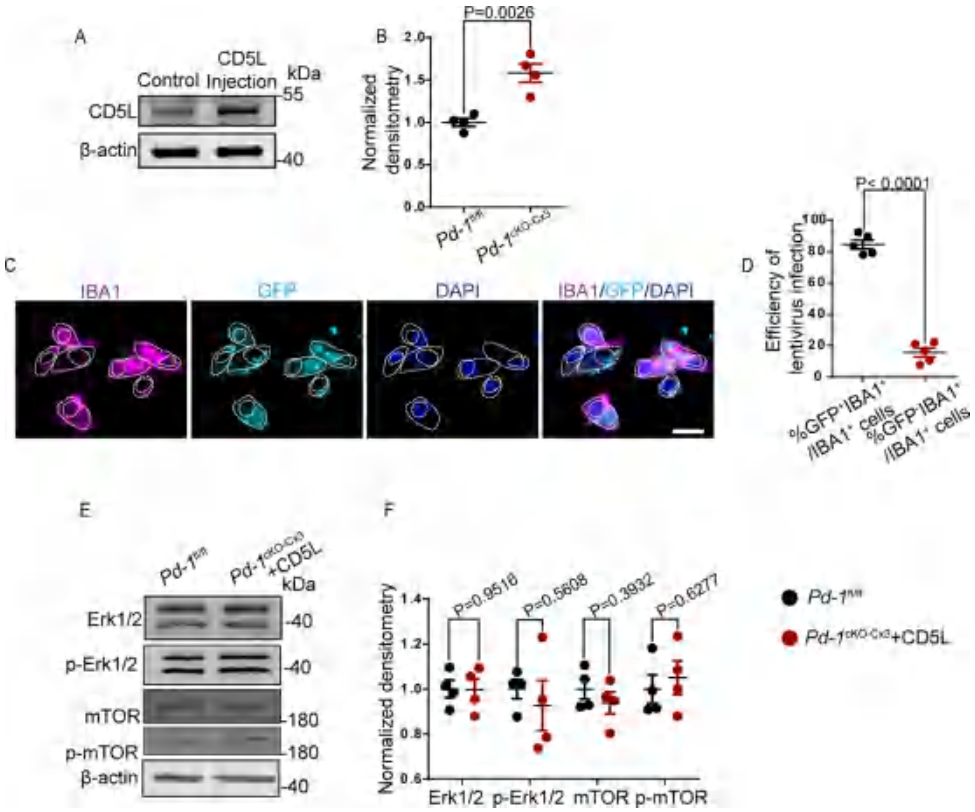

Extended Data Fig. 10 | The addition of CD5L rescues abnormalities of the Erk1/2–mTOR signaling pathway in *Pd-1*$^{cKO\text{-}Cx3}$ mice. (**A**) Western blot analysis showed that the level of CD5L protein was markedly increased after injected into the brain of mice. (**B**) Quantification of CD5L protein levels after CD5L injected into the brain of mice. n = 4 mice per group. (**C**) Representative images of IBA1 stained after 2 days of primary microglia transduction with lentiviral vector PCDH-3Flag-GFP-Cd5l. Scale bars, 10 μm. (**D**) The bar graph showed the efficiency of lentivirus infection. n = 5 mice per group. (**E**) WB showed that Erk1/2–mTOR signaling pathway returned to normal after adding CD5L protein to *Pd-1*$^{cKO\text{-}Cx3}$ microglia. (**F**) Quantitative analyses of Erk1/2–mTOR signaling pathway after adding CD5L protein to *Pd-1*$^{cKO\text{-}Cx3}$ microglia. n = 4 mice per group. For (**B**), (**D**) and (**F**) were analyzed using two-tailed unpaired t-test. Data are presented as mean ± s.e.m. for all statistical analyses.

nature portfolio

Corresponding author(s): Jianwei Jiao

Last updated by author(s): May 7, 2026

Reporting Summary

Nature Portfolio wishes to improve the reproducibility of the work that we publish. This form provides structure for consistency and transparency in reporting. For further information on Nature Portfolio policies, see our Editorial Policies and the Editorial Policy Checklist.

Statistics

For all statistical analyses, confirm that the following items are present in the figure legend, table legend, main text, or Methods section.

n/a	Confirmed
☐	☒ The exact sample size (*n*) for each experimental group/condition, given as a discrete number and unit of measurement
☐	☒ A statement on whether measurements were taken from distinct samples or whether the same sample was measured repeatedly
☐	☒ The statistical test(s) used AND whether they are one- or two-sided *Only common tests should be described solely by name; describe more complex techniques in the Methods section.*
☒	☐ A description of all covariates tested
☐	☒ A description of any assumptions or corrections, such as tests of normality and adjustment for multiple comparisons
☐	☒ A full description of the statistical parameters including central tendency (e.g. means) or other basic estimates (e.g. regression coefficient) AND variation (e.g. standard deviation) or associated estimates of uncertainty (e.g. confidence intervals)
☐	☒ For null hypothesis testing, the test statistic (e.g. *F*, *t*, *r*) with confidence intervals, effect sizes, degrees of freedom and *P* value noted *Give P values as exact values whenever suitable.*
☒	☐ For Bayesian analysis, information on the choice of priors and Markov chain Monte Carlo settings
☒	☐ For hierarchical and complex designs, identification of the appropriate level for tests and full reporting of outcomes
☒	☐ Estimates of effect sizes (e.g. Cohen's *d*, Pearson's *r*), indicating how they were calculated

Our web collection on statistics for biologists contains articles on many of the points above.

Software and code

Policy information about availability of computer code

Data collection	Immunofluorescence staining data was obtained from Zeiss LSM880. Live imaging data was obtained from NIKON A1R MP. Data from oxygen saturation level was obtained by Vevo F2 LAZR-X. Data from the blood flow level was obtained by RFLSI-ZW laser speckle contrast imaging system (RWD).
Data analysis	Data analysis were performed using GraphPad Prism 6.0 software, Imaris 9.7 software and Visualsonics® workstation suite (VevoLab).Most experiments were performed using three or more independent biological replicates. For comparisons between two groups, statistical significance was calculated using an unpaired two-tailed Student's t-test. For analyses involving two groups, One-way ANOVA was applied, followed by Dunnett's Test (comparing all groups to a control) or Tukey's Test (comparing all pairs of groups). For longitudinal or matched data, Repeated-Measures Two-Way ANOVA was employed, followed by Bonferroni's multiple comparisons test. For specific categorical data assessments, a two-tailed modified Fisher's exact test was used, with multiple hypothesis testing corrections applied via the Benjamini–Hochberg false discovery rate (FDR) procedure. Data distribution was assumed to be normal but this was not formally tested. All data were collected randomly, and mice were randomly allocated during the experiment. No statistical methods were used to pre-determine sample sizes but our sample sizes are similar to those reported in previous publications . No animals or data were excluded from the analysis.

For manuscripts utilizing custom algorithms or software that are central to the research but not yet described in published literature, software must be made available to editors and reviewers. We strongly encourage code deposition in a community repository (e.g. GitHub). See the Nature Portfolio guidelines for submitting code & software for further information.

Data

Policy information about availability of data

All manuscripts must include a data availability statement. This statement should provide the following information, where applicable:

- Accession codes, unique identifiers, or web links for publicly available datasets
- A description of any restrictions on data availability
- For clinical datasets or third party data, please ensure that the statement adheres to our policy

All statistical data supporting the conclusions of the study are provided in the 'Source Data' section. The raw data reported in this paper are accessible in NCBI's SRA (number: SRP530538).

Research involving human participants, their data, or biological material

Policy information about studies with human participants or human data. See also policy information about sex, gender (identity/presentation), and sexual orientation and race, ethnicity and racism.

Reporting on sex and gender	N/A
Reporting on race, ethnicity, or other socially relevant groupings	N/A
Population characteristics	N/A
Recruitment	N/A
Ethics oversight	N/A

Note that full information on the approval of the study protocol must also be provided in the manuscript.

Field-specific reporting

Please select the one below that is the best fit for your research. If you are not sure, read the appropriate sections before making your selection.

☒ Life sciences ☐ Behavioural & social sciences ☐ Ecological, evolutionary & environmental sciences

For a reference copy of the document with all sections, see nature.com/documents/nr-reporting-summary-flat.pdf

Life sciences study design

All studies must disclose on these points even when the disclosure is negative.

Sample size	Sample size for each experiment was noted in the Figure Legends. No statistical methods were used to predetermine sample sizes, but our sample sizes are similar to those reported in previous publications.
Data exclusions	No data were excluded from the statistical analysis.
Replication	All results were replicated in at least three cohorts of animals.
Randomization	Samples were assigned to different experimental groups based on their genotypes or treatment conditions, as indicated in the figure legends
Blinding	The experimenters confirmed the injection and craniotomy sites for all animals and were blinded to o behavioral outcome. All data analysis was performed by experimenters blinded to the animal grouping.

Reporting for specific materials, systems and methods

We require information from authors about some types of materials, experimental systems and methods used in many studies. Here, indicate whether each material, system or method listed is relevant to your study. If you are not sure if a list item applies to your research, read the appropriate section before selecting a response.

Materials & experimental systems

n/a	Involved in the study
☐	☒ Antibodies
☐	☒ Eukaryotic cell lines
☒	☐ Palaeontology and archaeology
☐	☒ Animals and other organisms
☒	☐ Clinical data
☒	☐ Dual use research of concern
☒	☐ Plants

Methods

n/a	Involved in the study
☒	☐ ChIP-seq
☐	☒ Flow cytometry
☒	☐ MRI-based neuroimaging

Antibodies

Antibodies used

The primary antibodies were listed as follows:
IB4(Vector Labs, B-1205, AB_2314661, 1:1000), CD68(Bio-Rad, MCA1957GA, AB_324217, 1:1000), IBA1(Wako, 019-19741, AB_839504, 1:1000), PD-1(Abcam, ab214421, AB_2941806, 1:500), F-actin(CoraLite®594-conjugated Phalloidin antibody, Proteintch, PF00003, 1:500), CD31(Biolegend, 102406, AB_312901, 1:500), Ki67(Abcam, ab15580, AB_443209, 1:1000), CD5L(abcam, ab45408, AB_726619, 1:500), HA (Cell Signaling Technology, 3724, AB_1549585, 1:1000), mTOR (Cell Signaling Technology, 2972, AB_330978, 1:1000), p-mTOR (Cell Signaling Technology, 5536S, AB_10691552, 1:1000), Phospho-p44/42 MAPK (Erk1/2)(Cell Signaling Technology, 9101S, AB_331646, 1:1000), p44/42 MAPK (Erk1/2)(Cell Signaling Technology, 9102, AB_330744, 1:1000), ZO-1(Invitrogen, 40-2200, AB_2533456, 1:300), Claudin5(Invitrogen, 352500, AB_87321, 1:300), GFAP(Dako, Z0334, AB_10013382, 1:1000), NeuN(Abcam, ab177487, AB_2532109, 1:1000), CX3CR1(Thermo Fisher Scientific, 14-6093-81, AB_467880, 1:1000), Synapsin1(Synaptic system, 106001, AB_2617071, 1:1000), Homer1(Synaptic Systems, 160003, AB_887730, 1:1000), P62(proteintech, 18420-1-AP, AB_10694431, 1:1000), LC3(proteintech, 14600-1-AP, AB_2137737, 1:1000), BrdU (Abcam, AB6326, AB_305426, 1:1000), CD36(novusbio, NB400-144, AB_920879, 1:300), GFP(MBL, D153-3, AB_591817, 1:1000), anti-PD-L1 mAb (BioX Cell, BE0101, AB_10949073), anti-PD-L2 mAb (BioX Cell, BE0112, AB_10950106).
The secondary antibodies were Alexa Fluor 488, Cy3 and Cy5(Jackson ImmunoResearch).

Validation

We only used antibodies that are commercially available and have been validated by the manufacturer and other laboratories. Prior to conducting the experiment, we validated these antibodies using positive and negative controls.

https://vectorlabs.com/products/biotinylated-gsl-i-isolectin-b4/
https://www.bio-rad-antibodies.com/monoclonal/mouse-cd68-antibody-fa-11-mca1957.html?f=purified
https://labchem-wako.fujifilm.com/us/product/detail/W01W0101-1974.html
https://www.abcam.com/en-us/products/primary-antibodies/pd1-antibody-epr20665-ab214421
https://ptglab.co.jp/products/CoraLite-594-Phalloidin-PF00003.htm
https://www.biolegend.com/en-gb/products/fitc-anti-mouse-cd31-antibody-120
https://www.abcam.cn/products/primary-antibodies/ki67-antibody-ab15580
https://www.abcam.com/en-us/products/primary-antibodies/cd5l-ct-2-antibody-ab45408
https://www.cellsignal.com/products/primary-antibodies/mtor-antibody/2972
https://www.cellsignal.com/products/primary-antibodies/phospho-mtor-ser2448-d9c2-xp-rabbit-mab/5536
https://www.cellsignal.com/products/primary-antibodies/phospho-p44-42-mapk-erk1-2-thr202-tyr204-antibody/9101
https://www.cellsignal.com/products/primary-antibodies/p44-42-mapk-erk1-2-antibody/9102
https://www.thermofisher.cn/cn/zh/antibody/product/ZO-1-Antibody-Polyclonal/40-2200
https://www.thermofisher.cn/cn/zh/antibody/product/Claudin-5-Antibody-clone-4C3C2-Monoclonal/35-2500
https://www.abcam.com/en-us/products/primary-antibodies/neun-antibody-epr12763-neuronal-marker-ab177487
https://www.thermofisher.cn/cn/zh/antibody/product/CX3CR1-Antibody-Polyclonal/14-6093-81
https://www.sysy.com/product/106011
https://www.sysy.com/product/160003
https://www.thermofisher.cn/cn/zh/antibody/product/P62-SQSTM1-Antibody-Polyclonal/18420-1-AP
https://www.ptglab.co.jp/Products/MAP1LC3B-Antibody-14600-1-AP.htm
https://www.abcam.com/en-us/products/primary-antibodies/brdu-antibody-bu1-75-icr1-proliferation-marker-ab6326
https://www.novusbio.com/products/cd36-antibody_nb400-144
https://bioxcell.com/invivomab-anti-mouse-pd-l1-b7-h1-be0101
https://bioxcell.com/invivomab-anti-mouse-pd-l2-b7-dc-be0112
https://www.mblbio.com/bio/g/dtl/A/index.html?pcd=D153-3
https://www.jacksonimmuno.com/catalog/products/711-546-152
https://www.jacksonimmuno.com/catalog/products/711-165-152
https://www.jacksonimmuno.com/catalog/products/711-175-152

Eukaryotic cell lines

Policy information about cell lines and Sex and Gender in Research

Cell line source(s)	HEK293FT cells were from ATCC (CRL-1573,).
Authentication	RRID:CVCL_0045, STR profiling.

Mycoplasma contamination	Cell lines were routinely tested for mycoplasma contamination by Mycoplasma PCR Detection Kit (Beyotime, C0301S).
Commonly misidentified lines (See ICLAC register)	No misidentified cell lines were used.

Animals and other research organisms

Policy information about studies involving animals; ARRIVE guidelines recommended for reporting animal research, and Sex and Gender in Research

Laboratory animals	Pd1fl/fl mice were generated by the Experimental Animal Center of the Institute of Zoology. Cd5lfl/fl mice were generated by Cyagen. Cx3cr1-Cre (Jackson Laboratories #025524), Cx3Cr1-CreER (Jackson Laboratories #021160), Ai14 (Jackson Laboratories #007914), Cx3cr1-GFP (Jackson Laboratories #005582), Tie2-Cre (obtained from Shanghai Model Organism), Tmem119-2A-CreERT2 (Cyagen #C001327) and Rosa26-iDTR (Cyagen #C001477) mice were maintained in a C57BL/6 background. Pd1cKO-cx3 mice were generated by crossing Pd1fl/fl mice with Cx3cr1-Cre and Cd5lcKO-cx3 mice were generated by crossing Cd5lfl/fl mice with Cx3cr1-Cre. Pd1fl/fl mice were crossed with Cx3cr1-CreER and Ai14 mice to obtain Pd1cKO-cx3ER::Ai14. To conditionally knock out the Pd1 gene in microglia, Pd1fl/fl mice were crossed with Tmem119-2A-CreERT2 and Ai14 mice to obtain Pd1cKO-TmemER::Ai14. To generate Tie2-cre::Ai14::Cx3cr1-GFP, Tie2-cre::Ai14 mice were crossed with the Cx3cr1-GFP mice line. Meanwhile, Tmem119-CreER::R26-DTR mice were obtained by crossing Tmem119-2A-CreERT2 mice with Rosa26-iDTR mice to establish microglia-deficient model mice. Experimental mice were analyzed at postnatal days 5, 7, 11, 13, 14, 20, and 40, comprising an equal number of males and females. Mice were subjected to random allocation, and all data collection and analysis were conducted by researchers blinded to the genotype.
Wild animals	This study did not involve wild animals.
Reporting on sex	Both males and females were included in the manuscript. The results for males and females were similar, with no sex differences.
Field-collected samples	The study did not involve samples collected from the field.
Ethics oversight	All animal experimental procedures were conducted in accordance with the Institutional Animal Care and Use Committee of the Institute of Zoology, Chinese Academy of Sciences(protocol number: IOZ-IACUC-2024-143).

Note that full information on the approval of the study protocol must also be provided in the manuscript.

Plants

Seed stocks	N/A
Novel plant genotypes	N/A
Authentication	N/A

Flow Cytometry

Plots

Confirm that:

☒ The axis labels state the marker and fluorochrome used (e.g. CD4-FITC).

☒ The axis scales are clearly visible. Include numbers along axes only for bottom left plot of group (a 'group' is an analysis of identical markers).

☒ All plots are contour plots with outliers or pseudocolor plots.

☒ A numerical value for number of cells or percentage (with statistics) is provided.

Methodology

Sample preparation	First, the mouse cerebral cortex from P11 was prepared as a single-cell suspension, filtered, and centrifuged. The cells were resuspended in a buffer containing fetal bovine serum, incubated with fluorescently labeled CD11b and CD45 antibodies, washed, and then adjusted to the desired cell concentration before being filtered; After calibrating the flow cytometer, exclude debris using forward scatter and side scatter, then set gates in the fluorescence channels. First, identify the CD11b-positive cell population, then select CD45-positive cells from this group (i.e., microglia), and finally sort them to the desired purity, collecting them into pre-chilled culture medium.

Instrument	BD FACSAria™ Fusion Flow Cytometer (BD fusion)
Software	FlowJo software
Cell population abundance	Take a portion of the sorted cells and perform fluorescence staining again (using the same CD11b and CD45 antibodies). Analyze the percentage of the target cell population among all detected cells using a flow cytometer, with a purity requirement of 90% or higher.
Gating strategy	Preliminary FSC/SSC threshold settings for microglia progenitor cells are based on the size and granularity characteristics of microglia. The forward scatter (FSC) signal obtained by flow cytometry reflects cell size, while the side scatter (SSC) signal reflects intracellular granularity. When setting thresholds, fragments with extremely low FSC and large cell clusters with extremely high FSC are first excluded. simultaneously excluding dead cells or other highly granular cells with excessively high SSC values. The final cell population with both FSC and SSC values within the moderate range is designated as the starting cells, thereby preliminarily enriching microglia and minimizing interference from unrelated cells.

☒ Tick this box to confirm that a figure exemplifying the gating strategy is provided in the Supplementary Information.